Acta Astronautica 224 (2024) 244–265

Contents lists available at ScienceDirect

Acta Astronautica

journal homepage: www.elsevier.com/locate/actaastro

Research Paper

Multidisciplinary design analysis and optimization of the aerodynamic shape of the SpaceLiner passenger stage

Tommaso Mauriello, Jascha Wilken *, Steffen Callsen, Leonid Bussler, Martin Sippel

German Aerospace Center (DLR), Space Launcher System Analysis (SART) of the Institute of Space Systems, Bremen, 28359, Germany

ARTICLE INFO

Keywords:
Multidisciplinary design analysis and optimization
Winged reusable launcher
Multi-objective aerodynamic and trajectory optimizations

ABSTRACT

The SpaceLiner is a futuristic concept of a suborbital space plane intended to provide ultra-fast intercontinental passenger transport, currently in pre-development at DLR-SART. Vehicles traveling at hypersonic speeds inevitably produce shock waves that are perceived at ground level as sonic booms, with associated disturbance of the overflown populations. The reduction of this disturbance, together with the decrease of the noise associated to the launch and ascent phase, is critical for a viable future operation of the SpaceLiner. The objective of this work is the redesign of the passenger stage aerodynamic shape in order to improve its atmospheric re-entry performance, in terms of a reduction of both the heat flux and the disturbance of the overflown populations. For this purpose, a MDAO methodology was developed with the tasks of (1) computing vehicle performance from a wing shape parametrization using fast estimation methods, (2) exploring the design space and (3) finding a new promising aerodynamic shape. First, a Python tool-chain was developed to compute vehicles performances from a wing shape parametrization using fast estimation methods. The tool-chain was then systematically exploited to explore the design space by means of parametric studies, whose results informed the implementation of the forthcoming optimization. Afterwards, the wing shape was optimized using a three-objective evolutionary algorithm that minimized the vehicle mass and maximized its lift-to-drag ratio and lift coefficient. Simplified trajectory optimizations were then run on the set of non-dominated solutions in order to identify the most performing configurations. Finally, multi-objective evolutionary trajectory optimizations were run for the most promising candidate along intercontinental point-to-point routes of interest. Comparisons with the previous design iteration showed a significant improvement in terms of a reduction of both reentry heat flux and population disturbance.

1. Introduction

1.1. The SpaceLiner concept

The SpaceLiner is a futuristic concept of a suborbital space plane intended to provide ultra-fast intercontinental passenger transport, breaking the technological barrier of commercial hypersonic travel (see Fig. 1).

The concept was first proposed in 2005 from the department of System Analysis Space Transportation (SART) of the DLR [1]. It consists of a rocket-powered, fully-reusable, suborbital winged TSTO designed for point-to-point ultra-long-haul commercial passenger transport, launching vertically and landing horizontally. On its reference mission, the SpaceLiner would capable of transporting 50 passengers from Europe to Australia in less than 90 min.

During the years the project has undergone several design iterations, with the SpaceLiner 7 being the most recent version of the vehicle, as well as the most detailed and elaborated conceptual design within the entire preliminary design phase. The SpaceLiner 7-1 was the first configuration whose aerodynamic shape was obtained, in 2011, from a fully automated optimization process [2,3], which targeted maximum lift-to-drag ratio on three different flight points on the reference trajectory. The optimization variables were a set of geometrical design parameters (nose radius, nose length, wing span, chord length, sweep angle, airfoil thickness) while a couple of geometrical and physical constraints were enforced (e.g. minimum lift, maximum stagnation point heat flux). The final solution was the result of a trade-off between the optima at the three flight points on the reference trajectory, and it pointed out the advantages of a single delta wing, which allows the simultaneous reduction of thermal loads, wave drag and structural loads, as well as of a reduction of the nose radius for a further reduction of wave drag. In this configuration the wing trailing-edge

* Corresponding author.
E-mail address: Jascha.Wilken@dlr.de (J. Wilken).

https://doi.org/10.1016/j.actaastro.2024.07.054
Received 11 April 2024; Received in revised form 3 July 2024; Accepted 29 July 2024
Available online 3 August 2024

Acronyms

AOA	Angle of attack
CAC	Computation of Aerodynamic Coefficients
COG	Center Of Gravity
COP	Center Of Pressure
DLR	German Aerospace Center
GGH	Grid Generation for HOTSOSE
HOTSOSE	Hot Second Order Shock Expansion
MDAO	Multidisciplinary Design Analysis & Optimization
MECO	Main Engine Cut Off
NSGA	Non-Dominated Sorting Genetic Algorithm
P2P	Point-to-Point
SART	Space Launcher System Analysis
SLOT	SpaceLiner Optimization Toolbox
SLP	SpaceLiner Passenger stage
STSM	Space Transportation System Mass
TBD	To Be Determined
	Conventional and Advanced spacecraft
TPS	Thermal Protection System
TSTO	Two Stage To Orbit

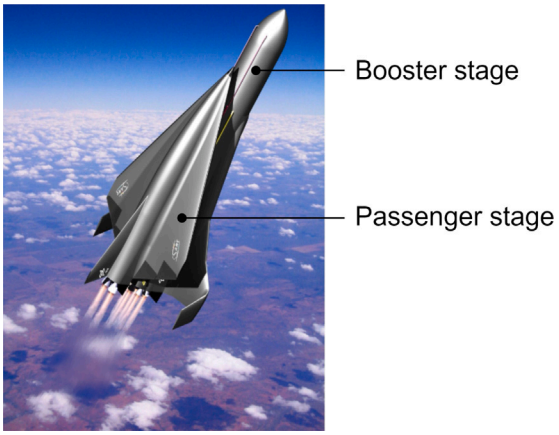

Fig. 1. Artist's impression of the SpaceLiner 7-3 ascent configuration.

was perpendicular to the fuselage, while in the following one (SL7-2) the wing was moved forward. At last, upon preliminary design of different subsystems and vehicle structures, the current SpaceLiner 7-3 configuration was obtained. For a comprehensive analysis of this configuration, see Ref. [4].

1.2. Hypersonic passenger transport concepts

In addition to the SpaceLiner, a number of other vehicles for hypersonic passenger transport have been studied or are currently in development. The most relevant ones are briefly outlined here.

- **Airbus**' *ZEHST* (Zero Emission Hyper Sonic Transportation) is an aircraft concept unveiled in 2011 and intended to fly at cruise speeds of Mach 4.5 using three different propulsive technologies: turbofans, rocket motors, and scramjets. It would be capable of transporting 20 passengers from London to New York in one hour, or Paris to Tokyo in three hours, lifting-off vertically and landing horizontally [5,6].
- **Destinus** is a private European aerospace company with headquarters located in Switzerland currently developing an air-breathing, hydrogen-fueled aircraft with horizontal take-off and landing. It would be capable of flying from Europe to Japan in 3 h, climbing at altitudes in excess of 30 km, reaching velocities of Mach > 5, and then gliding to its destination [7]. The *Destinus S* vehicle would be capable of transporting 25 passengers [8], while an advanced *Destinus L* configuration would target the transportation of up to 400 passenger with a cruise speed of Mach 6 [9].
- **Hermeus** is an American startup company from Atlanta, Georgia, developing *Halcyon*, an aircraft capable of transporting 20 passengers from New York to Paris in 90 min, flying at Mach 5 and at altitudes of 27 km. They are developing for this purpose the *Chimera* engine, capable of switching from turbojet to ramjet operations, as demonstrated in 2022 [10].
- **Reaction Engines Limited** is a British aerospace company which conceptualized the *LAPCAT A2*, a design study for a hypersonic speed jet airliner developed as part of the LAPCAT EU-funded program. It was designed to use liquid hydrogen as fuel and fly at Mach 5, transporting 300 passengers from Brussels to Australia in 4 h 40 min. The company stated that the concept could become a working vehicle within 25 years once there is market demand for it [11].
- **Radian Aerospace** is an American aerospace company based in Renton, Washington, developing *Radian One*, a single-stage to orbit vehicle with runway-like takeoff and landing. It is designed for a number of different capabilities, including rapid point-to-point passenger transport. Precise details are yet unknown [12].
- **Space Transportation** (Beijing Lingkong Tianxing Technology Co., Ltd.) is a Chinese company developing a space plane for space tourism and point-to-point travel. It would launch and land vertically, and it would be capable of traveling from Beijing to New York in one hour [13,14].
- **SpaceX** is currently developing *Starship*, a super heavy-lift launch vehicle which completed its 2nd integrated flight test on November 18th, 2023. Designed primarily to deliver payload to Mars and to the Moon, it would also be capable of performing point-to-point transportation by means of a vertical launch, a ballistic arc outside of the atmosphere and a vertical landing. For most international trips the travel duration would be under 30 min [15].
- **Venus Aerospace** is a Houston-based startup developing *Stargazer*, a horizontal take-off and landing aircraft that would be capable of transporting a dozen passengers at Mach 9, traveling from San Francisco to Tokyo in one hour, with a 2-hour turnaround between subsequent flights. It would employ a wave-rider design, propelled by a rotating detonation rocket engine and with an active TPS on the wing leading-edge [16].

1.3. Study motivation

Vehicles traveling at hypersonic speeds inevitably produce shock waves that are perceived at ground level as sonic booms, with associated disturbance of the overflown populations. The reduction of the population exposed to this disturbance, together with the decrease of the noise associated to the launch and ascent phase, is critical for a viable future operation of the SpaceLiner [17]. It is recalled that the sonic boom generation of the Concorde limited its operations to airspaces over water or uninhabited areas, and ultimately contributed to its retirement [18]. For this reason, a current study on the SpaceLiner concept [19] focused on assessing the viability of several P2P (point-to-point) intercontinental trajectories, which were optimized using a two-objective evolutionary algorithm (NSGA-III [20,21]) in order to minimize at the same time the re-entry peak heat flux and the overflown population disturbance.

Moreover, the same study compared the P2P performances of the SpaceLiner 7-3 with those of SpaceX's Starship vehicle, which is also expected to provide passenger transport capabilities. Two different approaches to minimize the overflown population disturbance were

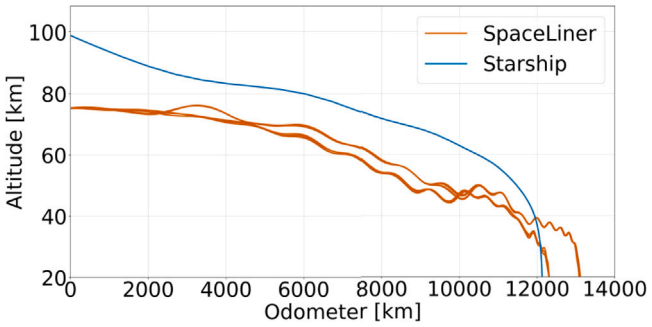

Fig. 2. Comparison of re-entry profiles (altitude - odometer) between SpaceLiner 7-3 and Starship along the route Brazil – India, from [19].

highlighted: whereas the SpaceLiner uses its large hypersonic lift-to-drag ratio (and the associated increased cross-range capabilities) to fly *around* populated landmasses, Starship flies *above* them, exploiting the fact that at altitudes in excess of 80 km the sonic boom disturbance reaching the ground can be neglected, as illustrated in Fig. 2.

This comparison suggested an interesting direction for the next design iteration of the passenger stage, the SLP8: re-designing the vehicle aerodynamic shape in order to be able to fly both mission types, depending on the geographic properties of the specific route. This would greatly increase the flexibility of the system and allow more routes to be served by the same vehicle.

1.4. Objectives

The objective of this work was thus the redesign of the passenger stage aerodynamic shape in order to be able to serve both gliding and ballistic/skipping mission types and ideally to reduce both the stagnation point peak heat flux and the disturbance of the overflown populations along P2P routes of interest.

2. Study rationale

2.1. Preliminary considerations

As a first approach, in order to find a more performing aerodynamic shape, one could attempt to simply run the same P2P trajectory optimizations outlined in [19] for various vehicle geometries. Unfortunately, these optimizations require days of run time to be completed on the available workstation (with 2x Intel Xeon Platinum 8260 L with 24 cores each) for an individual P2P route. For this reason, incorporating these optimizations as a function to be called within a broader optimization routine for a varying vehicle geometry (or even performing parametric studies for a limited set of geometry configurations) would result in an inefficient and impractical use of computational resources. Consequently, P2P optimizations shall be run only as a final validation step once promising vehicle configurations have been identified with a more structured approach, whose development is the core of this work.

The design of hypersonic vehicles for passenger transport applications is inherently a multidisciplinary challenge, as several technical disciplines are deeply interconnected: geometry, mass, aerodynamics, thermal protection, structure, propulsion, trajectory, stability etc. The identification of a new design capable of outperforming the previous SLP7-3 configuration requires therefore the development of a Multidisciplinary Design Analysis and Optimization (MDAO) framework, whose tasks can be stated as follows:

1. Quick assessment of vehicle performances from a parametrization of the aerodynamic shape.
2. Exploration of the design space.

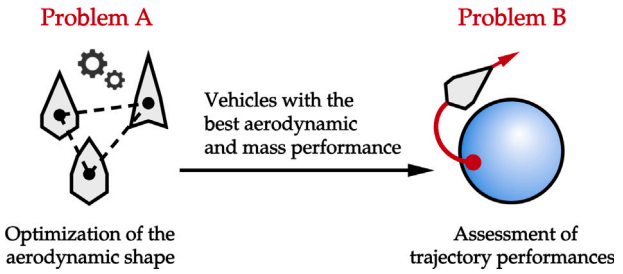

Fig. 3. Problem decoupling between aerodynamic shape optimization and assessment of trajectory performances.

3. Identification of a set of promising SLP8 configurations potentially outperforming the SLP7.

The utilization of MDAO in the field of space transportation has a long literature history. In this paper, an MDAO is applied on an innovative concept for a high-speed rocket-propelled point-to-point transportation system called SpaceLiner. In literature, MDAO techniques have been applied to a range of sub-problems like reusable launch vehicle architectures [22,23] and re-entry vehicle designs [24,25]. Common techniques to apply MDAO of launch systems involve metamodels, surrogate models and response surface methodologies [26,27]. Within the optimization, genetic algorithms are used to identify global optima in large design spaces, as presented in [22].

2.2. Problem decomposition

The complex design problem has been decoupled into two sub-problems in order to tackle it in a more effective way:

Problem A (wing-shape optimization), which concerns the optimization of the vehicle wing-shape in order to identify the vehicles with the best aerodynamic and inertial performances.

Problem B (trajectory optimization), which concerns the assessment of trajectory performances of the vehicles obtained from optimizing Problem A.

In general, optimizing two sub-problems, instead of an individual global problem, could lead to a sub-optimal global solution. Nevertheless, a partial coupling can be achieved by studying the interactions between the two sub-problems (i.e. the outputs of Problem A becoming the inputs Problem B). In particular, the vehicle characteristics that have a positive impact on trajectory performance can be identified, and then selected as optimization objectives for Problem A, as illustrated in Fig. 3.

In this way, it can be expected that the vehicles obtained from an optimization of Problem A will be the most performing when later optimized also for Problem B.

2.3. Exploratory studies

The initial step of this methodology is therefore the identification of the objectives of Problem A, i.e. what are the vehicle characteristics that shall be targeted in order to expect an improvement of trajectory performances? To answer this question, exploratory studies have been conducted on the two types of lifting re-entries: gliding and skipping trajectories (see Fig. 4).

Two different approaches have been employed:

1. Equations of motions (Refs. [28 to 35]) and heat-transfer relationships (Refs. [33] and [36]) have been used to understand, from an analytical standpoint, what are the main variables allowing a maximization of the re-entry range and a minimization of the G-loads, the heat fluxes and the heat loads, for both the types of re-entry.

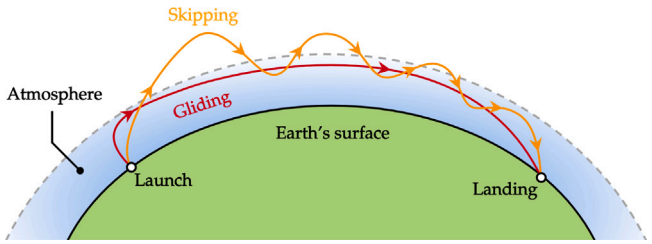

Fig. 4. Schematic illustration of the two types of lifting re-entries: gliding and skipping trajectories.

2. Simplified trajectories optimizations have been run for the SLP7 case with artificially modified aerodynamic and mass performance. These results helped assess, this time from a numerical standpoint, which vehicle performances have a beneficial effect on trajectory performance.

In addition, consistency between the two approaches constituted a crosscheck of these preliminary results. The specifics of these methodologies are omitted from the present discussion for the sake of brevity, but the interested reader can find an extensive discussion in [37]. As expected, they confirmed that for both gliding and skipping trajectories the re-entry performance is improved when the vehicle lift coefficient and lift-to-drag ratio are maximized, and when the vehicle drag coefficient and dry mass are minimized.

2.4. Overview of the MDAO methodology

Having established these preliminary results, it is now possible to describe the employed workflow to approach the problem of redesigning the SLP aerodynamic shape:

1. A software named SpaceLiner Optimization Toolbox (SLOT) has been developed to build a vehicle model from a geometrical parametrization of its wing shape. In particular, SLOT accesses a set of legacy DLR-SART numerical tools (based on fast estimation methods), formalizes the interactions between different disciplines and builds a coherent vehicle model to quickly estimate trimmed aerodynamics, mass and landing performance.
2. SLOT's capabilities have then been extensively used to perform parametric studies on thousands of different vehicle geometries, thereby enabling a comprehensive exploration of the design space. The obtained results provided a number of useful insights on Problem A, which were used (together with the results of the exploratory studies) to define the objectives of the forthcoming multi-objective wing-shape optimization, and eventually to simplify its implementation.
3. The vehicle wing shape has then been optimized, again exploiting SLOT capabilities, using the geometrical parameters defining the wing shape as input variables, and employing a three-objective evolutionary algorithm maximizing the vehicle lift coefficient and lift-to-drag ratio (evaluated at Mach 14) and minimizing its dry mass.
4. The set of non-dominated solutions of the wing-shape optimization have then been trajectory optimized along simplified routes (Problem B), in order to systematically assess trajectory performances and identify the most performing vehicles.
5. Finally, upon selection of the most promising candidate, the expected improvement in trajectory performances with respect to the SLP7 has been validated by comparing the two vehicles on P2P routes of interest by means of P2P trajectory optimizations.

Fig. 5 shows the block diagram of the MDAO methodology.

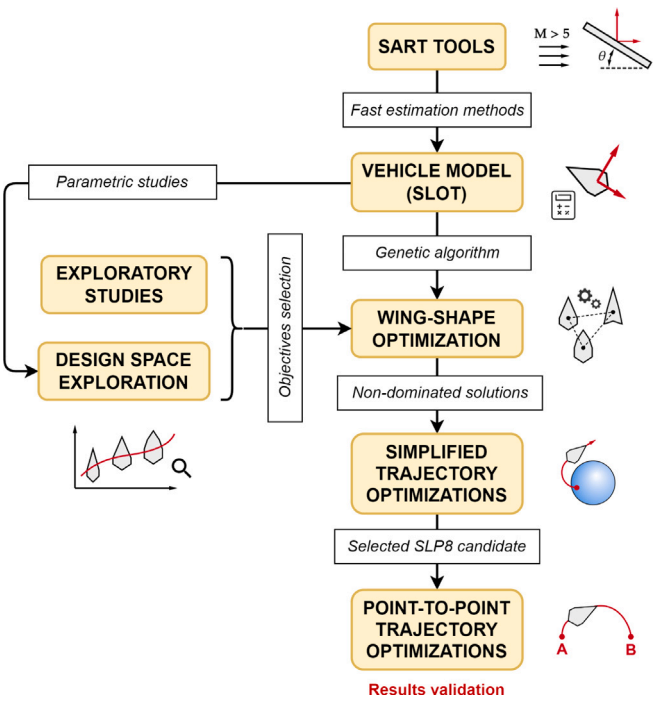

Fig. 5. Block diagram of the MDAO methodology.

3. Building the vehicle model

3.1. The SART numerical tools

At a pre-development level, a fast way of estimating vehicle performance is required. At DLR-SART there exist a number of numerical tools, developed through the years, to quickly address the different technical disciplines playing a role in the design of a launch vehicle. The following are the SART numerical tools that have been used in the context of this work:

1. **CAC** (Computation of Aerodynamic Coefficients) - Estimation of the vehicle aerodynamic coefficients in the sub- trans- and supersonic regime (Mach < 5) using handbook methods (similar to the DATCOM ones) [38].
2. **HOTSOSE** (Hot Second Order Shock Expansion) - Estimation of the vehicle aerodynamic coefficients in the hypersonic regime (Mach > 5) using local surface inclination methods [39], a common approach for hypersonic vehicles [30,40,41].
3. **GGH** (Grid Generation for Hotsose) - Mesh generation for HOTSOSE.
4. **STSM** (Space Transportation System Mass) - Generation of the vehicle mass model and estimation of the center of gravity (COG) position.
5. **TOSCA** (Trajectory Optimization and Simulation of Conventional and Advanced spacecraft) - 3 dof trajectory simulation [42].

3.2. Reference vehicle

The focus of the following investigation lies on the wing planform shape of the SpaceLiner passenger stage. However, in order to correctly assess the system performance, the vehicle first stage, the SpaceLiner Booster, and the fuselage of the orbiter are necessarily included in the system modeling. For reference, the key system data of the booster as well as fixed parameters from the passenger stage fuselage are given in Table 1.

Table 1
SpaceLiner Booster technical data. Values for passenger stage marked with "TBD" are subject to the optimization results and thus not defined a priori.

	Booster stage	Passenger stage
Dry mass	222 t	TBD
Total mass	1494 t	TBD
Length	82.3 m	65.6 m
Fuselage diameter	8.6 m	6.4 m
Engine cycle	Full-flow staged combustion	
Propellant type	Liquid oxygen and hydrogen	
Propellant mass	1272 t	232 t
Number of engines	10	2
Engines ISP, sea level	386 s	362 s
Engines ISP, vacuum	439 s	449 s
Thrust, sea level	2100 kN	2000 kN
Thrust, vacuum	2350 kN	2400 kN
Chamber pressure	15–17 MPa	
Return method	In-air capturing	Runway landing

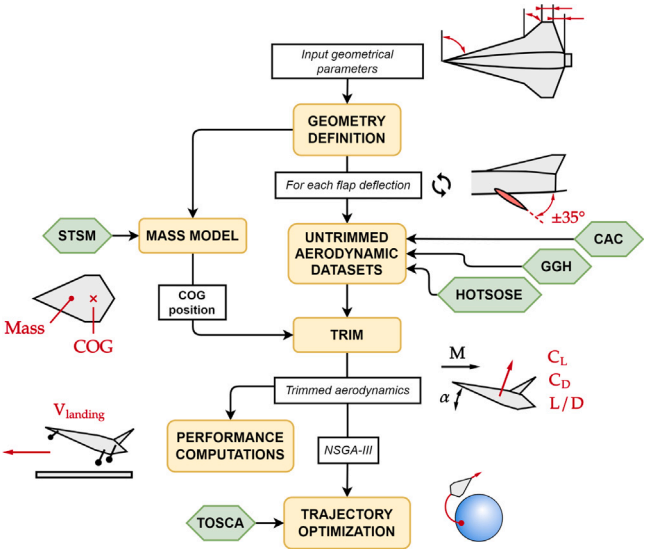

Fig. 6. Block diagram illustration of SLOT logic workflow. Green boxes indicate SART numerical tools.

3.3. The SpaceLiner optimization toolbox

An object-oriented Python tool-chain, named SpaceLiner Optimization Toolbox (SLOT), was developed in order to automatically access the SART tools and build a coherent vehicle model granting consistency between the various disciplines. In particular, from a geometrical parametrization of the vehicle wing shape, SLOT allows the estimation of the vehicle's:

- Pitch-trimmed aerodynamics as a function of the Mach number and the angle of attack.
- Mass model and COG position.
- Landing speed and configuration.

SLOT also provides extensive post-processing capabilities, in terms of computation of vehicle performances, that will be exploited to perform a comprehensive exploration of the design space, and upon completion of a vehicle's analysis, it can also be used to run trajectory optimizations. Fig. 6 illustrates the logic workflow employed within SLOT.

3.4. Coordinate system

Fig. 7 shows the employed coordinate system in the vehicle frame. The nose of the vehicle is located 2.38 m below the origin of the reference system. The x axis is parallel to the vehicle centerline and points towards the aft. The z axis is directed upwards, and the y-axis is thus constrained on a plane parallel to the wing, and directed towards the right wing.

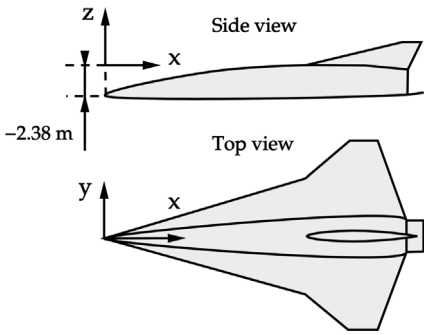

Fig. 7. Vehicle coordinate system.

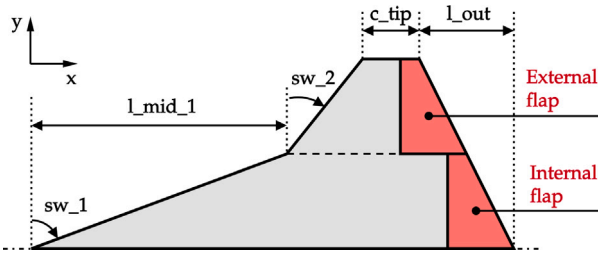

Fig. 8. Geometrical parameters defining the wing shape (half-configuration).

3.5. Geometry parametrization

The first step in any optimization procedure is the definition of the control variables. In our case, the control variables are the geometrical parameters defining the vehicle aerodynamic shape. The definition of the control variables is an important initial step in the MDAO methodology, as it regulates the trade-off between precision and required time of the optimization algorithm. Too many the geometrical parameters, and the design space would be too vast to explore, potentially preventing the identification of the optimum in a reasonable time. On the other hand, too little parameters would possibly imply a design space which does not include the optimum design.

Within this work it has been decided to modify the vehicle aerodynamic shape by altering only the wing shape. Therefore, both the airfoil type (modified NACA-66) and the fuselage shape have been kept unchanged. Since the propellant tanks are located inside the fuselage, this approach allows to exclude the propulsion subsystem, so the propellant loading, from the multidisciplinary problem. While simplified, this approach proved to be good enough to find a more performing aerodynamic shape.

Fig. 8 illustrates the five geometry parameters used to define a generic double-delta wing.

Moreover, just like for the SLP7 case, the wing is assumed to possess two wing flaps per side, which can be deflected up to ±35° for trim purposes (together with the body flap, which is also kept unchanged). Fig. 9 displays the admissible flap deflections. Note that the body flap can be deflected upward only up to −2.5° due to the space needed for the rocket engine nozzles.

When constraining the span-wise length of the two wing-flaps to be identical, the number of independent geometrical parameters (univocally determining the wing geometry) drops to four:

1. The first sweep angle `sw_1` [°].

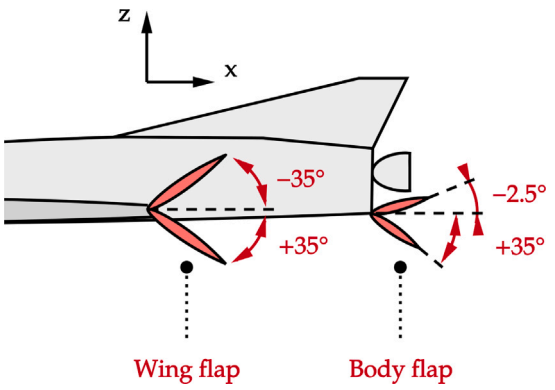

Fig. 9. Admissible flap deflections for the wing flaps and the body flap.

2. The second sweep angle `sw_2` [°].
3. The tip chord `c_tip` [m].
4. The outside chord `l_out` [m].

I.e. the `l_mid_1` parameter (mid-chord length) becomes a dependent variable. This choice of four parameters proved to be a good compromise between flexibility (a wide range of wing shapes can be analyzed) and simplicity (an overparameterization of the geometry would result in more complex optimization efforts).

Finally, SLOT is capable of identifying combination of geometrical parameters that would result in non-physical geometries. This functionality is extensively used when performing parametric studies or optimization routines (i.e. when the vehicle generation is automatic and not user-driven) to avoid analyzing inconsistent geometries.

3.6. Mass model

As previously stated, only the wing shape will be modified with respect to the SLP7-3 configuration. The methods employed to estimate the mass and COG position of the modified components will be presented hereinafter. Within STSM, the wing mass is estimated as follows, from [43]:

$$m_{wing} = 0.044 \cdot \left(m_{ref} \cdot n_z \cdot b \cdot \frac{S}{t} \right)^{0.584} \tag{1}$$

where the following parameters are specified in the STSM input file:

- n_z is the maximum normal load = 2.5 g.
- b is the wing structural span in m, defined starting from the fuselage side (and not from the fuselage centerline), and from half of the root chord, as illustrated in Fig. 10.
- S is the exposed surface area of the wing in m^2.
- t is the wing maximum airfoil thickness in m. It is the wing root thickness minus 30 cm of assumed TPS thickness, which is not load bearing and thus not included in the formula.

And where m_{ref} is equal to:

$$\left(m_{dry} + m_{prop,descent} + m_{prop,residuals} + m_{prop,reserve} \right) \cdot 1.25 \tag{2}$$

The wing COG is not computed within STSM but it must be assigned externally. Fig. 11 shows the approach used to estimate its position within SLOT.

First, the wing geometrical barycenter has been computed by breaking the wing shape down into elementary panels (triangles and rectangles) for which area and barycenter can be easily computed. Then, the x coordinate of the wing barycenter can be obtained as the weighted sum of the x coordinates of the individual panels, with the panels area as weights. For symmetry reasons, the wing barycenter y coordinate is zero (i.e. it lies on the symmetry axis), while the z coordinate has been set as identical to that of the wing leading edge (since the airfoil is symmetric, and neglecting the effect of the small angle of attack of the wing with respect to the fuselage).

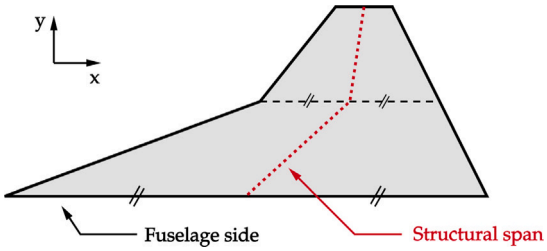

Fig. 10. Graphical definition of the wing structural span.

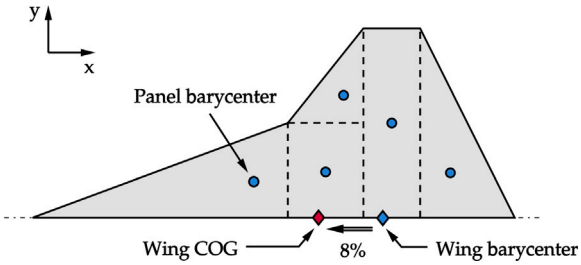

Fig. 11. Computation of the wing geometrical barycenter through subdivision of its surface in elementary panels, and 8% forward shift to estimate the wing COG.

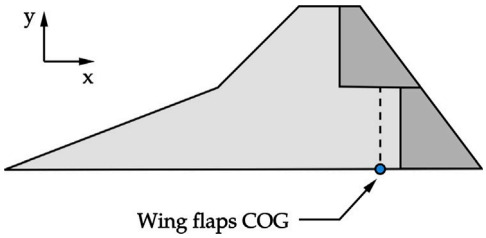

Fig. 12. Estimated position of the wing flaps COG.

Then, the wing COG position is obtained by shifting the geometrical barycenter by a factor of 8% in the x-direction towards the nose. This shift accounts for the increased mass at the wing leading edge due to the airfoil (and attached TPS) shape. This value of 8% allows to reproduce the difference between geometrical barycenter and COG position for the SLP7 geometry, and it has been enforced for all the vehicle geometries.

Then, the wing flaps mass is computed in STSM as follows, from [43]:

$$m_{flaps} = 0.4687 \cdot \left({m_{ref}}^{0.6667} \cdot (l + b)^{0.25} \right)^{0.903} \tag{3}$$

where:

- l is the passenger stage length in m.
- b is the wing span in m.

And where m_{ref} is computed as in Eq. (2).

The flaps COG along the x direction is assumed to be located at half the root chord of the external flap for vehicles with two identical flaps (see Fig. 12). This is a simplifying assumption motivated by the small contribution of the flaps to the overall vehicle mass model. Again, the y coordinate is zero for symmetry reasons, while the z coordinate is computed as the z coordinate of the wing COG minus 10 cm, as in the SLP7 case.

Finally, the TPS mass is computed by scaling the SLP7 TPS mass by the covered vehicle area (wing, fuselage and body flap bottom side), in

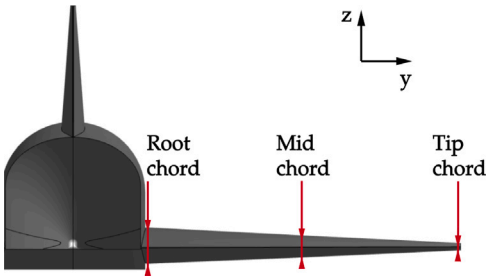

Fig. 13. Linearly decreasing wing thickness in the span-wise direction (rear view).

order to keep the same TPS mass per unit of covered area (15.38 kg/m^2) for all the vehicles, while the TPS COG is assumed to coincide with the wing COG.

The STSM output file also provides the variation of the vehicle inertial properties along the mission duration, including the varying position of the COG position. The value which is used for the trim computations is the average COG position between the beginning of the descent and the landing. The difference between these two positions originates from the consumption of cooling water used for the active thermal protection of the wing leading edge. In any case, due to the cooling water tanks being located in close proximity of the COG, the vehicle COG position does not change significantly during the atmospheric descent.

An optional additional input of the mass model estimation within SLOT is the uncertainty on the COG position. If this uncertainty is defined and different from zero, then two COG positions will be evaluated, associated respectively with the most negative and positive deviation from the computed COG position, according to the uncertainty. Trim performances will be evaluated for both the extreme cases, and the COG position leading to the worst trim performances (see following section) will be selected as a way of ensuring a robust design. Note that including a COG uncertainty increases the vehicle analysis run time as the trim interpolation must be performed twice. In the end this functionality has not been exploited during this work, but it could be easily be included in a follow-up study focused on finding robust designs.

The wing tip airfoil is kept identical to the SLP7 configuration (symmetric NACA 66 – 5.5%) as long as the tip chord thickness does not go below the minimum value of 35 cm. Thus, if the wing tip chord is less than the SLP7 case (6 m), the tip airfoil relative thickness is increased to maintain the minimum thickness value. Finally, the mid chord airfoil (wing chord associated to the separation line between the two wing flaps) is selected in order to maintain a linearly varying wing thickness, as shown in Fig. 13.

It is remarked that the vehicle landing mass corresponds to the vehicle dry mass plus the mass of the propellant residuals and the of propellant margin.

3.7. Computation of trimmed aerodynamics

Two different SART tools are used to compute the aerodynamic datasets, according to the flight regime:

- CAC is used to compute the aerodynamic dataset in the subsonic and supersonic regime. By default, the analyzed Mach numbers are from Mach = 0.25 up to Mach = 4, with a step size of 0.25.
- HOTSOSE is used to compute the aerodynamic dataset in the hypersonic regime (from Mach 5 onward). By default, the analyzed Mach numbers are from Mach = 5 up to Mach = 23, with a step size of 3.

Table 2
Reference flight profile (altitude-Mach number) employed for the aerodynamic computations.

Mach [–]	0.2	0.4	0.7	0.9	1.1	2.0	4.0
Altit. [km]	0.0	3.0	8.0	10.0	12.0	18.0	30.9
Mach [–]	6.0	10.0	14.0	18.0	20.0	22.6	
Altit. [km]	35.1	44.6	50.9	57.6	61.0	66.5	

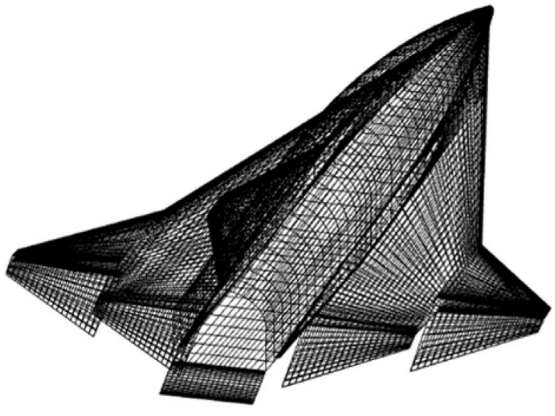

Fig. 14. Example of GGH vehicle mesh with downward deflected flaps.

The aerodynamic dataset of a vehicle contain the values of lift coefficient, drag coefficient and pitch moment coefficient as a function of the angle of attack and of the flight Mach number. For each geometry, these datasets are generated for five values of flap deflections: [-35°, -20°, 0°, +20°, +35°].

The analyzed angles of attack are identical for the CAC and HOTSOSE regime, and by default the range of angles of attack goes from α = 0° to α = 40° with a step size of 2°.

Table 2 shows the flight profile (Mach number – Altitude) used within CAC and HOTSOSE to compute the value of atmospheric density for each flight point. This flight profile corresponds to the reference SLP7 mission Australia–Europe, and it has been used as the reference for all the aerodynamic computations. The effects of a varying flight profile are usually small, but for the full P2P trajectory optimizations it should ideally be iterated to assure a consistent dataset.

Previous aerodynamic computations for the SLP assumed a fully turbulent hypersonic boundary layer up to Mach 18 (≈58 km of altitude) and a laminar boundary layer for higher Mach numbers and altitudes [41]. Conversely, within this work a fully turbulent boundary layer has been assumed for the whole entirety of the flight regime, which is the default conservative approach which was also used in [19].

Before running HOTSOSE, a mesh of the vehicle must be produced in order to apply the surface inclination method. For this purpose, GGH is run before HOTSOSE to generate the mesh files from the geometrical description of the vehicle. An example GGH generated mesh is shown in Fig. 14. The GGH input file is hence the one which is created according to the selected geometrical features of the vehicle (rather than the HOTSOSE one).

It is remarked that the computational effort between CAC and GGH+HOTSOSE is not balanced. Table 3 shows a comparison of the required run time for a test case (SLP7 geometry) on a single core. In the general case virtually all the run time is required by the combination GGH+HOTSOSE (GGH being almost instantaneous with respect to HOTSOSE, as well).

When possible, multiprocessing has then been exploited to shorten the required run time, e.g. assigning the analysis for each flap deflection to different cores when a single vehicle is being analyzed.

CAC and HOTSOSE use as reference point for the pitch moment coefficient the origin of the coordinate system ([0, 0, 0]). Then, once

Table 3
Run time breakdown for the aerodynamic computations on a test case on a SART workstation.

	N. of flap deflections	N. of Mach numbers	Angles of attack	Run time
CAC	1	16	21	0.5 s
HOTSOSE	1	7	21	54 s

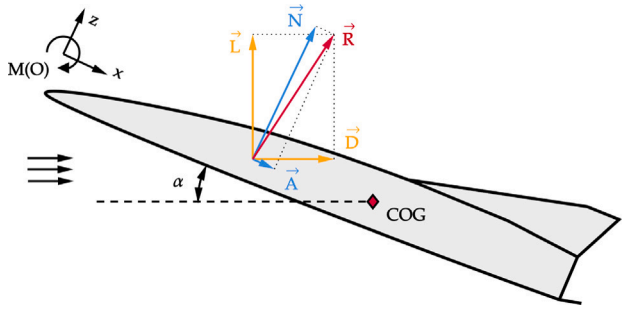

Fig. 15. Vehicle free body diagram for the shift of the moment reference point.

the COG has been computed from STSM, or once a COG position has been imposed by the user, the pitch moment curve must be translated around the COG in order to proceed with the trim computations. Fig. 15 shows the vehicle free body diagram used to shift the pitch moment reference point from the origin to the COG.

First, the resultant aerodynamic force R is projected in the vehicle reference frame (N is the normal component in the z-direction, while A is the axial component in the x-direction):

$$\begin{bmatrix} N \\ A \end{bmatrix} = \begin{bmatrix} \cos(\alpha) & \sin(\alpha) \\ -\sin(\alpha) & \cos(\alpha) \end{bmatrix} \begin{bmatrix} L \\ D \end{bmatrix} \tag{4}$$

The moment with respect to the COG is then computed as:

$$M(G) = M(O) + R \times (O - G) = M(O) + N \cdot G_x - A \cdot G_z \tag{5}$$

Where O indicates the origin of the vehicle reference frame ([0, 0, 0]), while G indicates the COG position. Scaling the equation, the relationship between the aerodynamic coefficients is obtained:

$$\frac{M(G)}{\frac{1}{2}\rho V^2 LS} = \frac{M(O)}{\frac{1}{2}\rho V^2 LS} + \frac{N}{\frac{1}{2}\rho V^2 LS} \cdot G_x - \frac{A}{\frac{1}{2}\rho V^2 LS} \cdot G_z \tag{6}$$

$$\rightarrow \; C_m(G) = C_m(O) + C_n \cdot \frac{G_x}{L} - C_a \cdot \frac{G_z}{L} \tag{7}$$

Once the information of the COG-centered pitch moment coefficient is available for the set of computed flap deflections, it is possible to trim the vehicle. Aerodynamic performances of an untrimmed vehicle are in fact of low to no importance, as an acceptable solution in terms of vehicle geometry should be able to fly its re-entry trajectory with zero pitch moment in all the flight points. Figs. 16–18 show how the trim interpolation is performed for each value of angle of attack and Mach number (in this example M = 14 and $\alpha = 10°$, for a test geometry).

First, the pitch-moment curve is interpolated with a spline of second order between the five flap deflections for which aerodynamic computations have been carried out. The interpolated curve is then numerically solved (the method `broyden1` [44] within the `scipy` library [45] in Python has been used in this case) to find the value of angle of attack granting zero pitch-moment, as illustrated in Fig. 16.

Then, the lift and drag coefficient curves are also interpolated, and the values associated to the computed flap deflection are retrieved, as illustrated in Figs. 17 and 18.

Finally, the lift-to-drag ratio is computed from the ratio of the two interpolated values of lift and drag (i.e. the lift-to-drag curve is not interpolated).

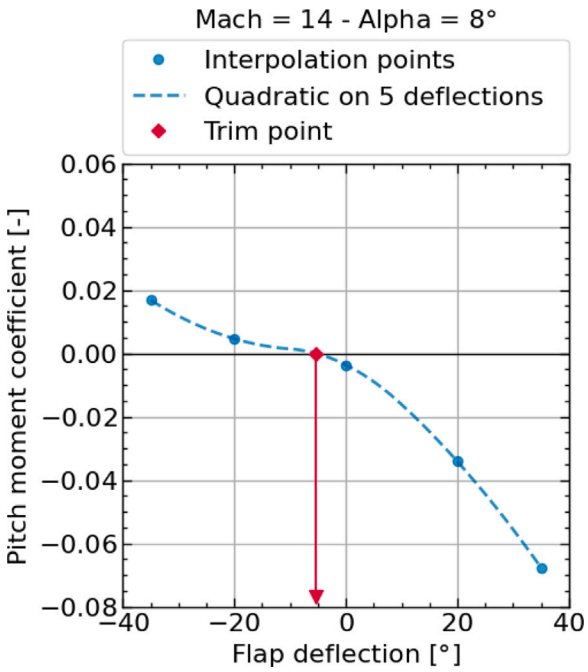

Fig. 16. Computation of flap deflection granting zero pitch moment.

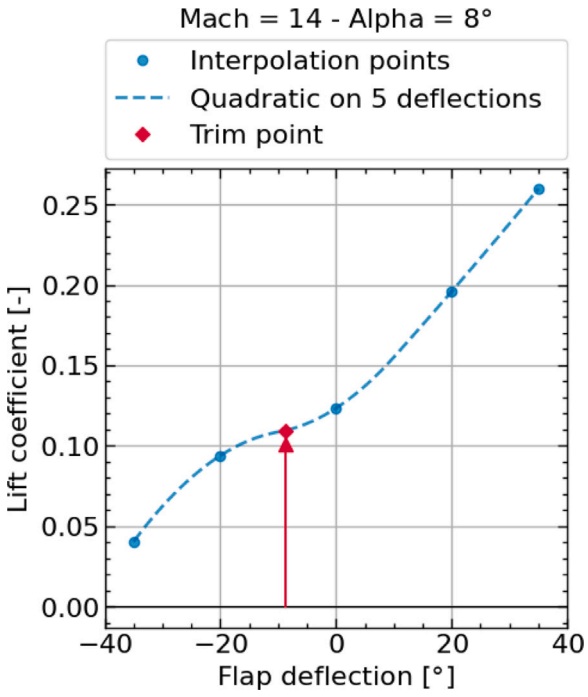

Fig. 17. Retrieval of the lift coefficient associated to the zero pitch moment flap deflection.

If no solution is found at the first step (i.e. there is no flap deflection granting null pitch-moment coefficient) the vehicle is non-trimmable at this specific value of angle of attack and Mach number. The flap deflection granting the lowest pitch moment coefficient is then selected, and the residual pitch-moment coefficient is stored (since in theory one could extend the vehicle trimmability by means of additional control actuators, e.g. a reaction control system, thus the information on the minimum residual pitch moment coefficient could be useful for further analyses).

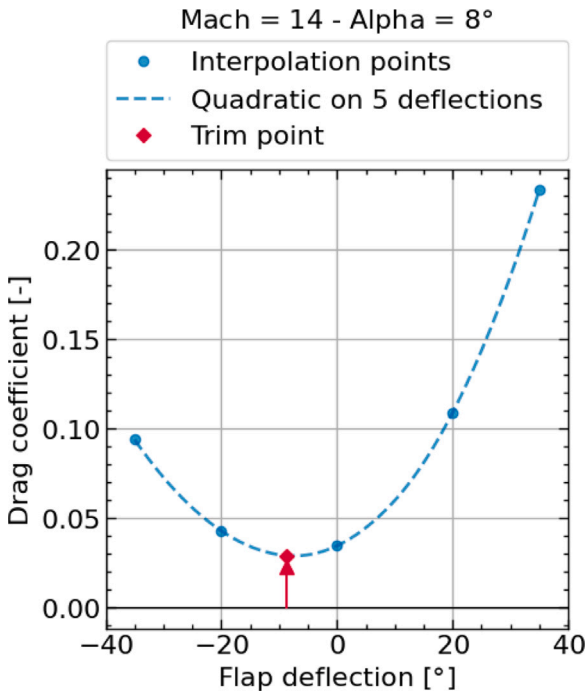

Fig. 18. Retrieval of the drag coefficient associated to the zero pitch moment flap deflection.

Table 4
Main performance metrics for the SLP7 configuration.

Max L/D at Mach 14	3.66
Max CL at Mach 14	0.81
Landing mass	137.65 t
MECO mass	151.46 t
Landing speed	78.72 m/s
Landing AOA	10°
Landing flap deflection	14.26°
Landing is stable	False
Is flyable	True
Flyable score M<5	95%
Flyable score M>5	68%
Stability score M<5	15%
Flyable score M>5	73%

Even though it is not a strict requirement, it is preferred to have stable trimmed configurations (negative slope of the pitch-moment curve, or center of pressure being located after COG). For this reason, the slope of the pitch moment curve in correspondence of the trim flap deflection is also computed and stored for further stability considerations of the trimmable points.

3.8. Computation of vehicle performances

A wide number of performance metrics are computed once the vehicle trimmed aerodynamics are available. These metrics have been used to explore the design space in detail, and they also served as objectives and constraints in the optimization routines. In the end, trade-offs between vehicles (at least before running trajectory optimizations) will be based on these performance metrics. Table 4 displays the main performance metrics for the SLP7 geometry.

It is remarked that, for a given Mach number, the maximum lift coefficient is associated to the maximum trimmable angle of attack (in the range of angles of attacks under study), while the maximum lift-to-drag ratio is always associated to smaller values of angles of attack (around 8°).

The landing configuration is defined by the following values of Mach number and angle of attack:

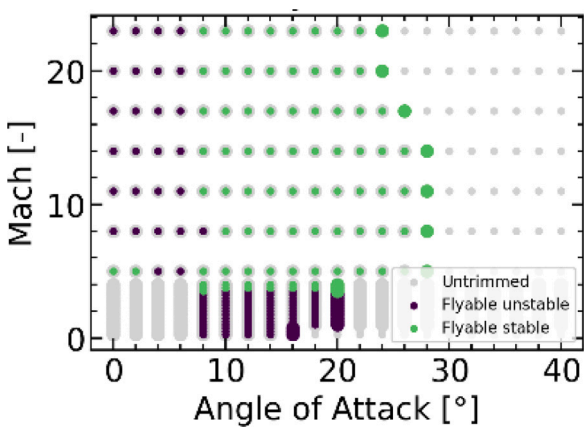

Fig. 19. Result of the trim analysis for the SLP7 configuration.

- Mach 0.25 (the smallest Mach number computed by CAC). At the sea level this Mach number corresponds to a vehicle speed of $0.25 \cdot 343 \cong 86$ m/s, which is considered an acceptable landing speed.
- The trimmable angle of attack granting the largest lift coefficient below a maximum value of 10°.

The landing speed is then computed from an equilibrium between the lift and the gravitational force at landing:

$$mg_0 = \frac{1}{2}\rho V^2 S C_L(\alpha) \tag{8}$$

$$\rightarrow V = \sqrt{\frac{2mg_0}{\rho S C_L(\alpha)}} \tag{9}$$

It is remarked that the increased lift at landing due to ground effect or to leading-edge vortices (typically generated by delta wings at subsonic speeds and moderate angles of attacks [46]) have not been taken into consideration in this analysis, for both simplification and conservative purposes. On the other hand, no specific margin for maneuverability at landing is included. However, the aforementioned factors as well as the moderate reference angle of attack for landing are considered sufficient to allow for adequate maneuverability.

A vehicle is said to be *flyable* if there exists at least one trimmable angle of attack for each Mach number under study (in our case from Mach 23 to Mach 0.25). If this is not the case, than there exists at least one Mach number for which the vehicle cannot be trimmed, so that the atmospheric re-entry cannot be performed, i.e. the vehicle is not flyable. The flyable score is defined as the percentage of flyable points with respect to the number of analyzed flight points. Fig. 19 shows the result of the trim analysis on the SLP7 geometry, as a function of the angle of attack and Mach number. Colored points indicate flyable flight points, so those reachable passing only through trimmable states. In particular, green dots indicate pitch-stable flight points, and violet dots the unstable ones.

The difference in point density between above and below Mach 5 is due to the different resolution employed within CAC and HOTSOSE in terms of number of analyzed Mach numbers.

3.9. Limitations

The herein performed multidisciplinary optimization of the wing shape of a hypersonic vehicle necessarily covers a large range of physically complex phenomena across multiple engineering disciplines. Due to finite computational resources, it is impractical to assess the vehicle with the most detailed or sophisticated models, and even these models have notable uncertainties in their results. Instead, faster engineering approaches are chosen, believed to deliver sufficiently accurate results

to identify promising solutions meriting further investigation. While these methods include simplifications and assumptions, they represent a good balance between detail and computational efficiency.

Specifically, the mass estimations methods are based on empirical formulas that capture the general trends but cannot account for the details of an actual implementation. The tool used for aerodynamic coefficients below Mach 5, CAC, is based on superposition of the contributions of fuselage, wing and stabilizer components. It relies on a combination of simplified theoretical methods (as e.g. lifting line theory) with empirical relationships and thus is not (always) able to reflect complex aerodynamic phenomena such as the interaction between separate components. As a tool based on surface inclination methods, HOTSOSE is able to deliver surface pressure distributions on the analyzed geometry, however, an analysis of the flow field in the volume around the body is not possible and thus the interaction between different components can also not be captured. The implemented methods are Mach number dependent and increasingly more accurate with higher Mach numbers. Furthermore, at the time the mass model and aerodynamic datasets are generated, the optimized trajectories are not available. Thus, any beneficial (or detrimental) effect the aerodynamic shape has on specific subsystems is not inherently considered. This specifically affects the vehicle structure and TPS. A convergent structural mass estimation is assured by constraining the mechanical loads (n_z and p_{dyn}) during the later trajectory optimization. With regard to the TPS mass, the estimated mass is based on the area density of the TPS of the SLP7. As the stagnation point heat fluxes encountered by the SLP8 candidate, as shown in Section 5.3, are significantly lower than for the SLP7, this approach is considered conservative.

These simplifications and assumptions introduce bias to the solution. Complex phenomena, like the lift enhancing double-vortices system formed in subsonic flight for double delta wings or shock–shock interactions in hypersonic flight, cannot readily be accounted for with the methods chosen herein. Both the under and overestimation of certain performance parameters will lead to bias and potentially the selection of suboptimal or non-feasible designs. As a plausibility check, the set of non-dominated solutions is subjected to expert judgement after their trajectory performance has been evaluated. The thus identified candidate still contains the potential bias of the methodology but is deemed promising enough to warrant further evaluation. The efficient methodology implemented herein also allows iterative updates based on later evaluation with more sophisticated models.

4. Design space exploration

SLOT's capability of providing a comprehensive analysis of trimmed vehicle performance in under a minute serves as a powerful tool in a preliminary design phase.

The first task it has been assigned to is the exploration of the design space of Problem A, in terms of the relationship between vehicle performance and input geometrical parameters. To do so, parametric studies have be performed by means of a systematic variation of the wing shape input geometrical parameters and the subsequent computation of the associated vehicle performance; thousands of different vehicle geometries have been studied in this way, resulting in a comprehensive exploration of the design space which provided a number of useful insights on the design problem at hand.

4.1. Significance of performance metrics computed at Mach 14

A first parametric study has been performed by varying the wing input geometrical parameters in the following ranges:

1. First sweep angle `sw_1` ∈ [60°, 80°], step size 2°.
2. Second sweep angle `sw_2` ∈ [40°, 80°], step size 10°.
3. Tip chord `c_tip` ∈ [8 m, 32 m], step size 6 m.
4. Outside chord `l_out` ∈ [−10 m, 20 m], step size 5 m.

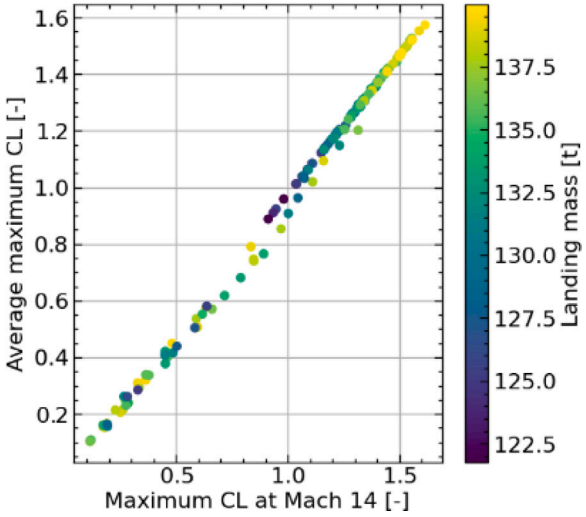

Fig. 20. Relationship between maximum lift coefficient at Mach 14 and average maximum hypersonic lift coefficient. The colormap indicates the vehicles' mass.

Within this parametric variation vehicles with excessively large wings, and thus dry mass, could be obtained. Vehicles with a landing mass over 150 t were excluded from the following analysis, in order to avoid analyzing too massive vehicle configurations (the SLP7 landing mass is 137.65 t). This parametric study resulted then in 1210 different vehicle geometries upon mass filtering. Fig. 20 displays one result of this parametric study. The plot, where each dot represents a different vehicle geometry, illustrates the relationship between the maximum lift coefficient at Mach 14, and the average hypersonic maximum lift coefficient (i.e. the average, over the hypersonic Mach numbers, of the maximum trimmable lift coefficients).

It is evident that there is almost a linear relationship between the two metrics. This result holds also for the drag coefficient and for the lift-to-drag ratio. Conversely, this correlation does not hold as well for lower or higher hypersonic Mach numbers (the same relationship has been investigated also at Mach 5 and Mach 23).

This indicates that hypersonic performance evaluated at Mach 14, for the vehicle geometries under study, can be considered representative of the average hypersonic performance. Thus, during the aerodynamic optimization of the wing shape, analyzing the whole hypersonic regime and then computing the average value of an aerodynamic performance (either the maximum lift coefficient, drag coefficient or lift-to-drag ratio) at each Mach number can be substituted with a simple evaluation of the aerodynamic performance at Mach 14. Since, as previously discussed, hypersonic computations (in HOTSOSE) are the most time demanding step during a vehicle analysis, this approach reduces the required computational time by about 80%, while still allowing a comparison of vehicles in terms of hypersonic performance.

4.2. Relative position of SLP7 in the design space

It was then possible to run a new parametric study covering a larger set of differing vehicle geometries by restricting the aerodynamics computation in the hypersonic regime to Mach 14. This time the wing input geometrical parameters have been varied in the following, more refined, ranges:

1. First sweep angle `sw_1` ∈ [55°, 80°], step size 1°.
2. Second sweep angle `sw_2` ∈ [40°, 85°], step size 3°.
3. Tip chord `c_tip` ∈ [3 m, 24 m], step size 3 m.
4. Outside chord `l_out` ∈ [0 m, 20 m], step size 4 m.

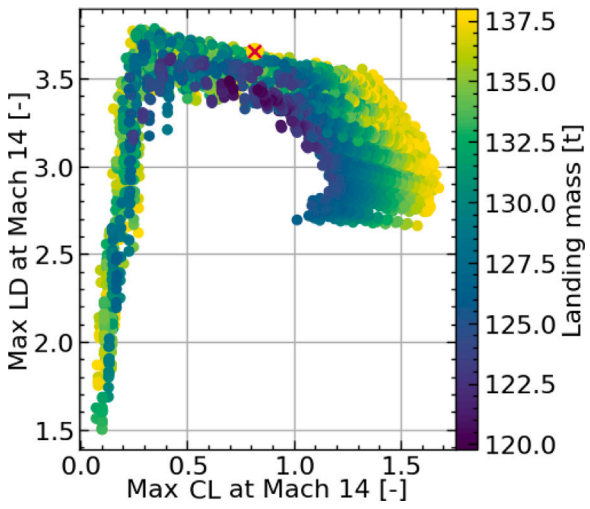

Fig. 21. Relationship between lift-to-drag ratio, lift-coefficient (both at Mach 14) and landing mass for 10904 different vehicle geometries. Red cross indicates SLP7 performance.

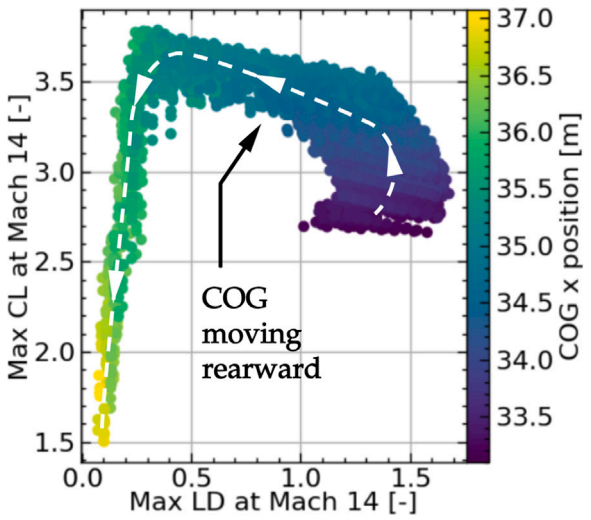

Fig. 22. Coupled variation of lift coefficient and lift-to-drag ratio as a function of the COG position. Dashed line indicates increasing values of COG axial position.

This time vehicles with a landing mass greater than 140 t were filtered out, in order to steer the analysis towards the interesting parts of the design space, i.e. focusing on vehicles mostly lighter than the SLP7, resulting in 10904 different vehicle geometries upon mass filtering. Fig. 21 is one notable result of this parametric study, displaying the relationship between the three main parameters for all these vehicles: the aerodynamic performance at Mach 14 (lift coefficient and lift-to-drag ratio), and the landing mass. Each dot represents a trimmed configuration with a landing speed of less than 100 m/s, while the red cross indicate the SLP7 performance.

As it can be observed, the SLP7 configuration lies on the two-dimensional pareto front in terms lift-coefficient and lift-to-drag ratio maximization (as a matter of fact, it lies also on the three-dimensional pareto front of these three metrics). This proves two points:

1. That the SLP7 is indeed a good design as it maximizes, for its values of lift coefficient and vehicle mass, the hypersonic lift-to-drag ratio (it was in fact optimized to perform gliding re-entry trajectories [2,3]).
2. That SLOT is capable of effectively explore the design space and correctly locate the SLP7 within it.

4.3. Trade-off between lift coefficient and lift-to-drag ratio

Preliminary studies showed how an increase in both the lift-to-drag ratio and in the lift coefficient is beneficial in terms of trajectory performance. In particular, maximizing the lift-to-drag ratio is mostly beneficial for a gliding re-entry, while during a skipping re-entry a large lift-coefficient allows to fly at higher altitudes thereby reducing both the re-entry heat flux and the disturbance of the overflown population. Unfortunately, a vehicle that maximizes both metrics does not exist, and a compromise will need to be found. The objective of this section is to show where this trade-off originates from.

Fig. 22 displays the same data presented in Fig. 21 but colored according to the vehicles COG axial position. As it can be observed, the COG x coordinate is a clear indicator of the vehicle location along the distribution, as indicated by the dashed line.

As it will be now explained, it is not really the COG position which is relevant, rather the wing position with respect to the fuselage, of which the COG x coordinate is a direct indicator. To understand this behavior, it is in fact necessary to understand how, for vehicles with differently positioned wings, the relative position between the COG and the COP changes.

The COP position is not an available information from the HOTSOSE output. Although it could be computed from the output pressure distribution, its location can also be quickly estimated using the same relationships previously introduced to shift the pitch moment reference point and enforcing the aerodynamic moment at the COP to be zero, as per its definition, given in Eq. (5):

$$M(G) = M(P) + R \times (P - G) \tag{10}$$

$$\rightarrow C_M L = \emptyset - C_N \cdot (P_x - G_x) + C_A \cdot (P_z - G_z) \tag{11}$$

$$\rightarrow P_x = G_x + \frac{C_A \cdot (P_z - G_z) - C_M \cdot L}{C_N} \tag{12}$$

Note that in this equation there are actually two unknowns: the x and z coordinates of the COP. In order to compute the x position of the COP, an assumption must be made on its z-position. Two approaches appear reasonable:

- COP z position coinciding with the COG z position. This would imply that the axial force does not contribute to the aerodynamic moment.
- COP z position coinciding with the wing z position. This would imply that most of the aerodynamic force is originated by the wing, which seems reasonable, at least as the angle of attack increases.

In the end, it has been observed that both the assumptions provide similar results in terms of COP x location, and finally the first assumption has been retained as it better agreed with upcoming results.

Under these assumptions, the COP movement can then be computed as a function of the angle of attack and of the Mach number. As an example, Fig. 23 displays the results for one arbitrary vehicle geometry (named `SLP8V-E03624`) at Mach 14.

A non-monotonic movement of the COP with respect to the angle of attack is observed. After an initial sharp movement from the fore to the aft section, as the angle of attack increases, there is a forward movement of the COP (towards the nose) followed by a rearward movement (towards the aft section), with the COP position eventually stabilizing for large values of angle of attack.

This behavior was investigated by analyzing the pressure contour which can be output from HOTSOSE at a specific flight point. At 0° angle of attack the pressure distribution on the wing is concentrated its leading edge, thus the wing produces almost no lift and only drag. On the other hand, the fore section of the fuselage is exposed to the flow

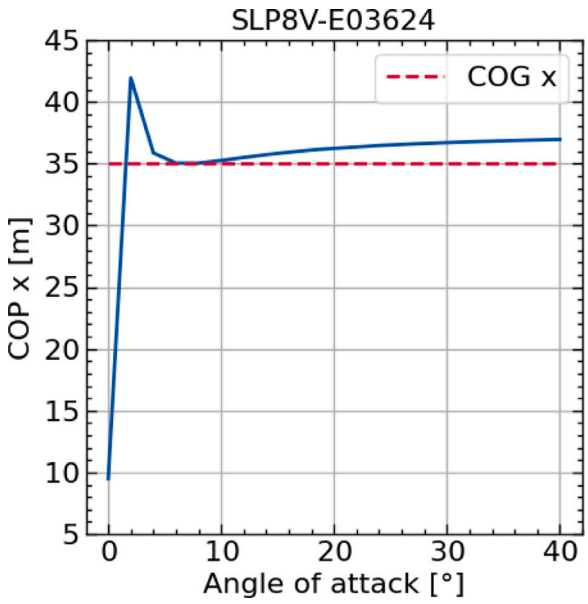

Fig. 23. COP position over angle of attack for vehicle SLP8V–E03624 at Mach 14.

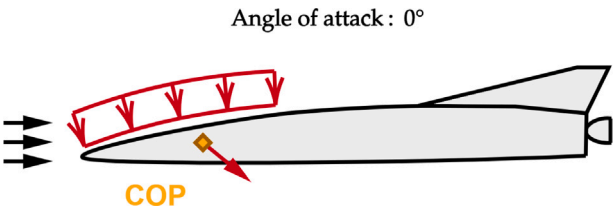

Fig. 24. Schematic illustration of COP location at 0° of angle of attack, resulting from the negative pressure distribution generated on the fuselage.

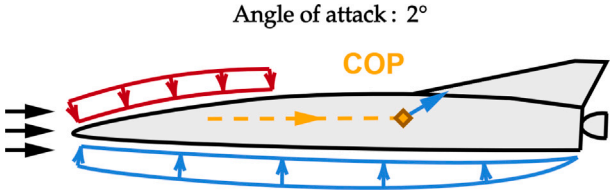

Fig. 25. Schematic illustration of the COP movement from 0° to 2° of angle of attack, resulting from the different pressure distributions over the fuselage and the wing.

and it has a non-null pressure distribution, producing a downward force which explains both the negative lift coefficient observed at 0° of angle of attack, and the extremely forward position of the COP, as illustrated in Fig. 24.

At 2° of angle of attack a non-null pressure distribution develops also on the wing bottom surface. The overall lift coefficient is now positive, meaning that the pressure distribution on the wing more than compensates the downward force exerted by the pressure on the fuselage fore section. The negative lift generated by the fuselage is compensated by the pressure distribution on the forward part of the wing, so that the positive lift generated on the aft wing section shifts the COP towards the rear of the vehicle (see Fig. 25).

From 2° to 8° of angle of attack the negative lift coefficient contribution from the fuselage gradually fades away (the fuselage gets more and more shaded from the incoming hypersonic flow, with a minimal pressure contribution coming from the expanded flow above the fuselage), while the pressure distribution below the wing leading edge predominates over the rest of the wing, so that the COP shifts towards the vehicle nose (see Fig. 26).

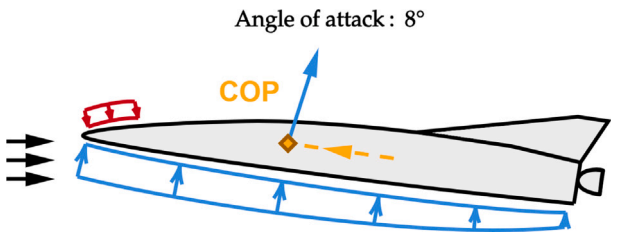

Fig. 26. Schematic illustration of the COP movement from 2° to 8° of angle of attack, resulting from the different pressure distributions over the fuselage and the wing.

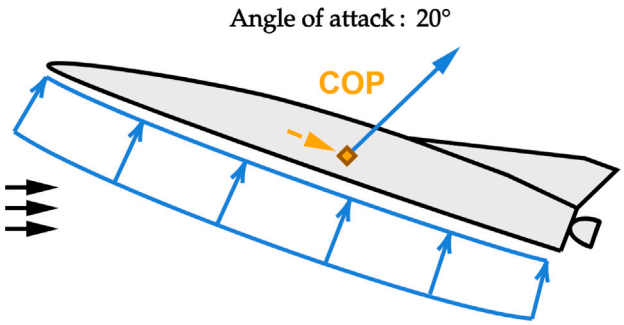

Fig. 27. Schematic illustration of the COP movement at large values of angle of attack, resulting from the pressure distribution mostly concentrated on the fuselage bottom.

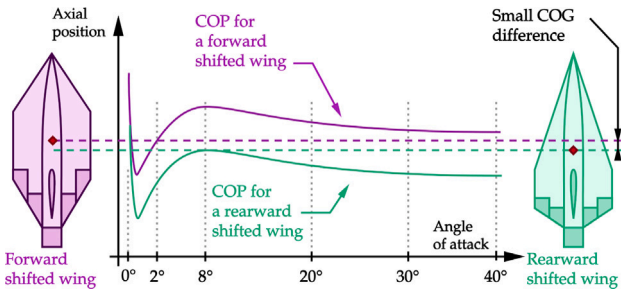

Fig. 28. Schematized behavior of COP movement with angle of attack for forward and rearward shifted wings, and relative COG positions.

Finally, at higher angles of attack the pressure more uniformly distributes over the wing bottom side, and even though the aft section is associated to lower values of the pressure coefficient, the wing area is here larger and the aerodynamic contribution of this section grows. For this reason, the COP moves once again towards the rear of the vehicle (see Fig. 27).

What is remarkable is that for different vehicles the illustrated COP movement with respect to the angle of attack is almost identical, while what really changes is the relative position between the COP and the COG. This relative movement is schematically illustrated in Fig. 28, for vehicles with forward shifted and rearward shifted wings. Although the wing COG moves as the wing is shifted rearward, the vehicle COG is almost constant as the vehicle mass is mostly contained within the fuselage (the maximum COG variation in Fig. 22 is 2.5 m, i.e. 4% of the vehicle length). On the other hand, even if the variation of the COP with the angle of attack has a similar shape for different vehicles, the relative position between this curve and the COG position will change according to the wing position. In Fig. 28 the two COP curves are thus represented identical in shape but vertically translated, according to the associated wing position.

This COP behavior implies that:

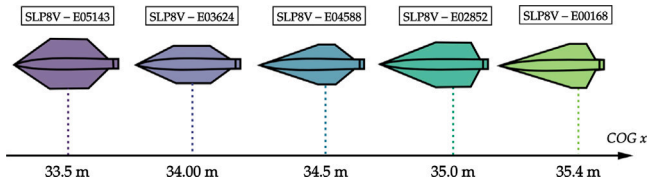

Fig. 29. Vehicle geometries with increasing COG axial position sampled from the parametric study.

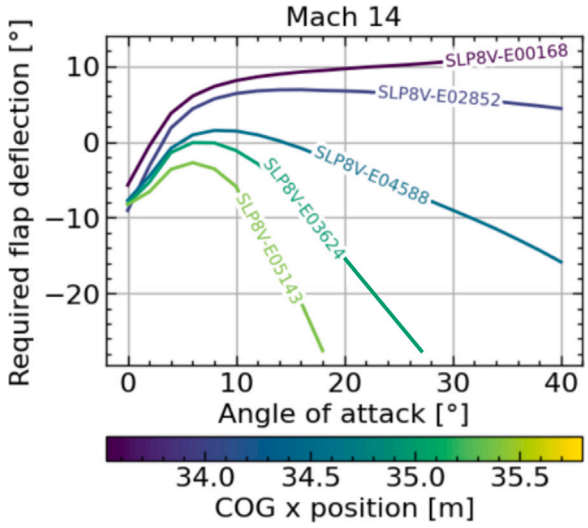

Fig. 30. Variation of the required flap deflection as a function of the angle of attack at Mach 14, for vehicles with increasing COG axial position.

- All the vehicles require a negative flap deflection at 0° of angle of attack to compensate the aerodynamic moment produced by a negative lift coefficient acting in front of the COG.
- Vehicles with forward shifted wings are hypersonically unstable from small values of angles of attack onward (COP in front of the COG).

Both these properties are indeed observed for the vehicles under study.

It must then be considered that the COP movement determines the moment arm $(P - G)$ of the aerodynamic force, but then the aerodynamic moment will be the (cross) product of this moment arm with the aerodynamic force. The required flap deflection will be proportional to the aerodynamic moment to be compensated; for this reason, even if the COP position appears to stabilize for larger values of angle of attack, it can be expected that the required flap deflection will keep on increasing as the aerodynamic force will keep on doing so. The actual variation of the required flap deflection with the angle of attack can be explored by analyzing vehicles of the parametric study with increasing COG x positions (indicating wings that are more and more rear-shifted). Fig. 29 presents the five vehicles that have been selected for the following comparison.

Fig. 30 displays the variation of the required flap deflection as a function of the angle of attack for these vehicles with differently positioned wings, at Mach 14.

As it was previously remarked, all of them require negative flap deflections at 0° of angle of attack (in the hypersonic regime). Moreover:

- For forward shifted wings (e.g. vehicle SLP8V−E00168), the initially negative flap deflection quickly reaches the 0° value at small angles of attack (around 2°). Afterwards, the COP position moves in front of the COG, the configuration becomes unstable, and the flap deflections turn positive. Even if the COP then moves back towards the COG (without crossing it), the aerodynamic force, steadily increasing with the angle of attack, forces the flap deflections to increase even if the aerodynamic moment arm decreases. Moreover, the effective angle of attack of the flap α_f is the sum of the flap deflection η and the vehicle angle of attack α:

$$\alpha_f = \eta + \alpha \tag{13}$$

  Indicating that positive flap deflections, being downward, are more effective, as the flaps are fully immersed in the incoming hypersonic flow, while negative flap deflections have a smaller effective angle of attack with respect to the flow and thus they are less effective. This greater effectiveness of positive flap deflections contributes to the slower growth of the required flap deflection with angle of attack for vehicles with forward shifted wing.
- For rearward shifted wings (e.g. vehicle SLP8V−E05143), the initial negative flap deflection is larger in magnitude (as the arm of the aerodynamic moment to compensate is now greater). For this reason, even if the COP movement changes direction also in this case, it will reverse even before reaching the COG line. The minimum flap deflection will not therefore be 0°.

Note how for vehicle SLP8V−E03624 the required flap deflection is zero at 8° of angle of attack. This means that at this flight point the COP and COG coincide (as it can be cross-checked observing Fig. 23, which validates the assumption of $COP_z = COG_z$ to solve Eq. (12), at least for this specific case), resulting in a trimmed configuration with no flap deflection, delivering the maximum aerodynamic efficiency for that angle of attack.

As the wing is shifted more and more towards the rear of the vehicle, the distance between the COG and the COP becomes so large that:

- The flap deflections are large even at low values of angle of attack.
- The maximum trimmable angle of attack is very small (even less than 10°).

These vehicles are therefore associated to both a low lift coefficient and lift-to-drag ratio, and they are represented by the left branch in Fig. 22 (green and yellow dots, i.e. large COG x position).

If the absolute value of the required flap deflection is plotted instead, as shown in Fig. 31, it becomes evident how much faster it grows for vehicles with rear-shifted wings. That is because, after the most forward position of the COP is reached (at around 8°), even if the aerodynamic force is increasing with the angle of attack, the aerodynamic moment-arm decreases for forward-shifted wings (the COP moves towards the COG) while it increases for the rearward-shifted ones (the COP moves away from the COG).

Finally, considering that the wing baseline maximum lift-to-drag ratio (i.e. with 0° flap deflection) will be always located at values of around 8°, it is concluded that:

- Vehicles with forward shifted wings have a zero flap deflection at lower values of angle of attack, and greater flap deflections in correspondence of the wing baseline maximum lift-to-drag ratio, i.e. they are “wasting” aerodynamic performance, as they are forced to use large flap deflections at their most efficient angle of attack. On the other hand, they can fly at larger values of angle of attack as the required flap deflections grow at a slower rate with the angle of attack, since the COP moves back towards the COG thereby reducing the aerodynamic moment arm.
- Vehicles with rearward shifted wings have a smaller maximum angle of attack, as their required flap deflection quickly reaches the maximum allowable value (both the aerodynamic moment arm and the aerodynamic force increase with the angle of attack). But the angle of attack associated to the minimum flap deflection (even if it may not be 0°) is closer to the angle of attack delivering the largest lift-to-drag ratio of the baseline wing shape. These vehicles can therefore maximize their aerodynamic efficiency.

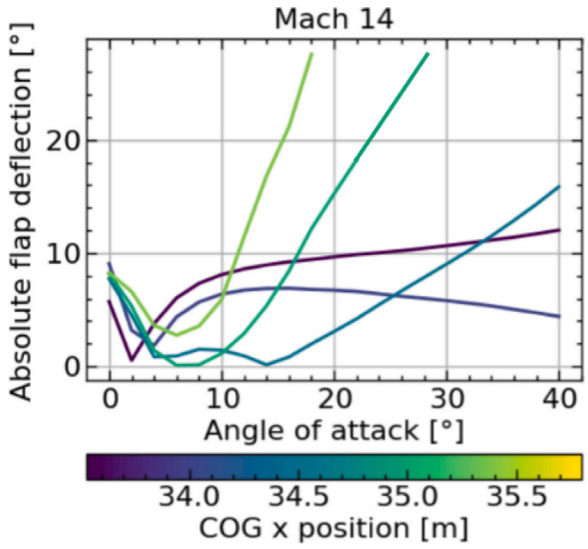

Fig. 31. Variation of the absolute flap deflection as a function of the angle of attack at Mach 14, for vehicles with increasing COG axial position.

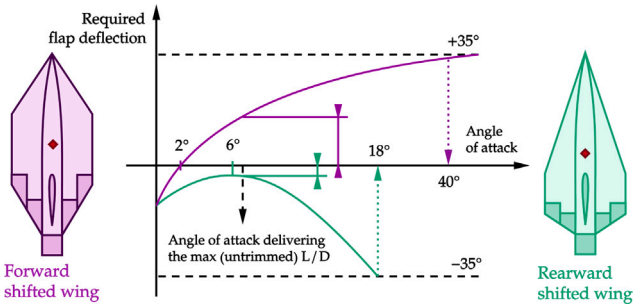

Fig. 32. Trade-off between maximum lift coefficient and lift-to-drag ratio dictated by the wing position.

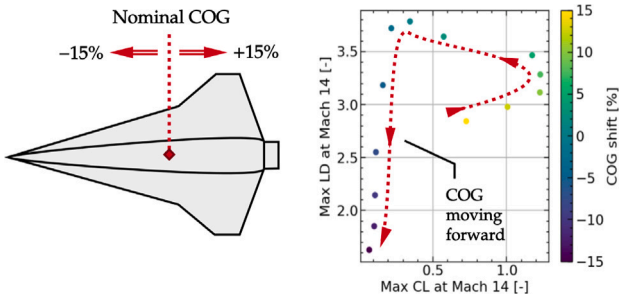

Fig. 33. Coupled variation of maximum lift-to-drag ratio and lift coefficient at Mach 14 as a function of the COG axial position of the vehicle.

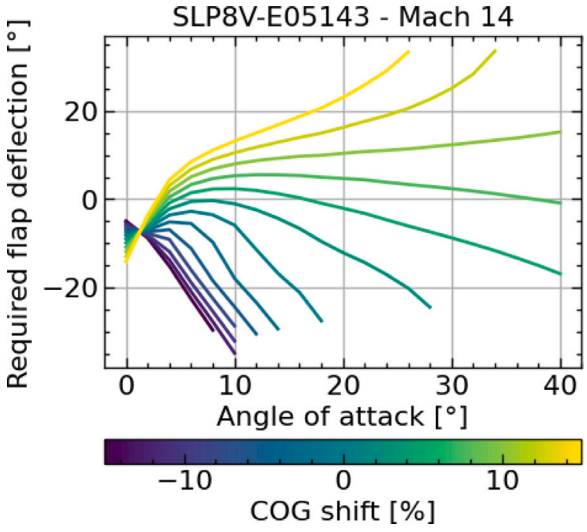

Fig. 34. Effect of the COG axial position on the required flap deflection as a function of the angle of attack, for vehicle SLP8V−E05143 at Mach 14.

This is schematically illustrated in Fig. 32.

It is now possible to understand how the trade-off between maximum lift coefficient and maximum lift-to-drag ratio comes down to the relative position between the COP and COG, which ultimately depends on the wing position, of which the axial position of the vehicle COG is a direct indication.

Therefore, a vehicle presenting a good compromise between lift coefficient and lift-to-drag ratio would display a variation of the required flap deflection as a function of the angle of attack which would be in between the two curves in Fig. 32; around 0° flap deflection at ≈ 8° of angle of attack, so to maximize the baseline wing lift-to-drag ratio, and then a slowly growing amplitude of the required flap deflection, so to be able to fly at large angles of attack and therefore achieve large values of maximum lift coefficient.

A cross-check of these results is that the same trend observed in Fig. 22 appears also when assessing the effect of a COG shift on an individual vehicle geometry, as illustrated in Fig. 33.

When several vehicles are being analyzed, the COG position is almost fixed and the COP moves with the wing. Conversely, in this case the COP is fixed with the wing, at the COG is artificially shifted. That is why the observed trend is actually in the opposite direction with respect to Fig. 22. Fig. 34 shows how the required flap deflection as a function of the angle of attack changes as the COG is moved, displaying the same behavior that was observed in Fig. 30 for different vehicles.

It is observed that all the curves intersect in the same point, which represents a pair angle of attack-flap deflection which is independent of the COG position. This occurs at the zero-lift angle of attack, which is around 1° (it is reminded that the lift at 0° of angle of attack is negative due to the contribution of the negative pressure distribution on the fuselage). In this configuration, the aerodynamic moment is at a minimum (the drag moment arm being small), so any axial movement of the COG does not really change the aerodynamic moment around it, and thus the flap deflection required to compensate it is also constant.

4.4. Correlation between the four objectives

It has been previously stated that the re-entry performance is improved when the vehicle lift coefficient and lift-to-drag ratio are maximized, and when the vehicle drag coefficient and dry mass are minimized. Exploiting the result that aerodynamic performance at Mach 14 are representative of the average hypersonic performance, this leaves us with four optimization objectives (3 aerodynamic performance at Mach 14, and one mass metric). Unless specified otherwise, all following aerodynamic performance are evaluated at Mach 14.

The results of the parametric studies have been used to show that the these four performance metrics are strongly correlated between each other, indicating that one of them can be excluded from the objectives of the wing-shape optimization. In particular, a statistical analysis has been carried out to understand how the values of the drag coefficient are distributed for vehicles with similar values of the other metrics. Specifically, for each vehicle of the parametric study, vehicles with similar lift coefficient, lift-to-drag ratio, and landing mass (within a range of ±1%) were grouped together. Subsequently, the statistical properties of each group were determined in terms of drag coefficient distribution, as illustrated in Fig. 35. In particular, for each group,

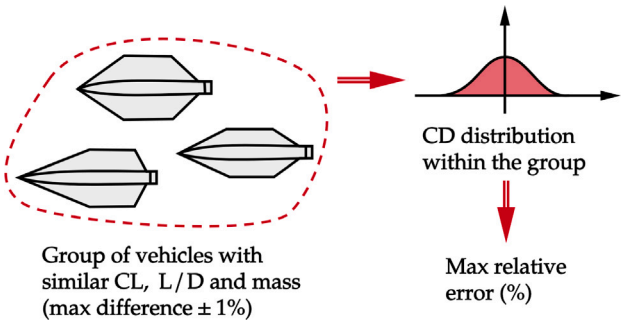

Fig. 35. Schematization of the statistical analysis on drag coefficient distribution.

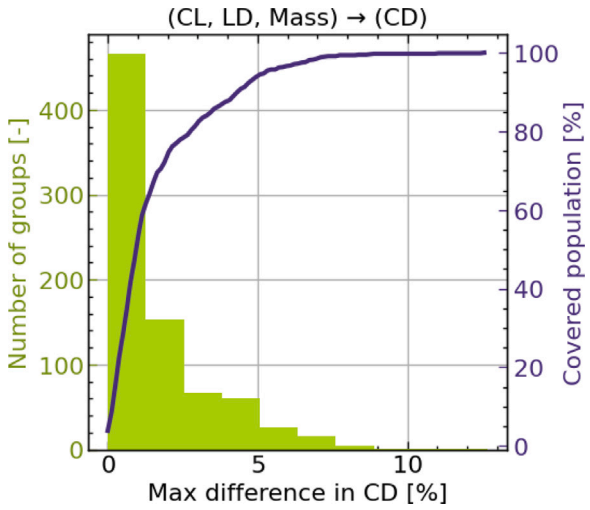

Fig. 36. Distribution of relative percentage error in drag coefficient for vehicles with similar values of lift coefficient, lift-to-drag ratio and mass (within ±1%).

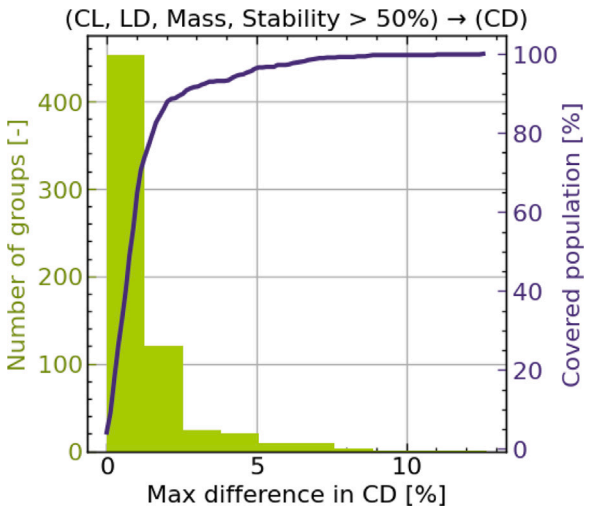

Fig. 37. Distribution of relative percentage error in drag coefficient for vehicles with similar values of lift coefficient, lift-to-drag ratio and mass (within ±1%) which are also mostly stable in the hypersonic regime.

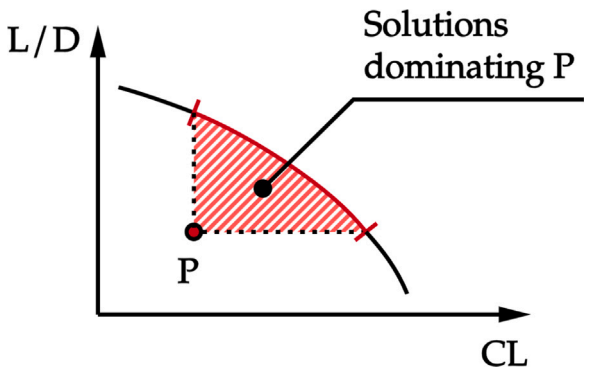

Fig. 38. The dominated solution P cannot be the one with the best re-entry performance.

the maximum deviation from the mean value of the distribution was computed in terms of relative error (in percentage).

If, when analyzing a vehicle, no other vehicle exists with the three metrics within 1% of difference, then the vehicle is not considered for the statistical analysis (otherwise that group would be composed of only one vehicle, and a perfect correlation would be displayed). Fig. 36 displays the result of the statistical analysis, in terms of distribution of the maximum percentage difference in drag coefficient.

As it can be observed, for around 60% of the cases the maximum drag coefficient difference (from the mean value of the group) is less than 1.25%. And for virtually all the cases the maximum error is below 10%.

Restricting even more the analysis to only stable vehicles at the maximum trimmable angle of attack in the hypersonic regime, the difference drops below 5% for more than 95% of the population, as shown in Fig. 37.

Since this error is of the same order of magnitude of the variation of the input parameters (1%), it is concluded that for the vehicles of interest (stable in the hypersonic regime) the drag coefficient metric can be considered as a dependent variable of the other three (lift coefficient, lift-to-drag ratio and mass), thus simplifying the wing-shape optimization by removing one optimization objective. Nonetheless, even when not restricting the analysis to hypersonically stable vehicles, an error which mostly lies below 5% could be acceptable given the decrease of computational effort associated to a reduction of optimization objectives.

5. Optimization

When considering the three remaining objectives separately, they must be either maximized or minimized, which implies that the best vehicle is located on the pareto front of the non-dominated solutions. To prove this point it is possible to consider, without loss of generality, the case of only two objectives to be maximized (i.e. lift coefficient and lift-to-drag ratio), with the mass metric being identical for all the vehicles under consideration. Using a *reductio ad absurdum*, it can be assumed that the vehicle with the best trajectory performances does not belong to the pareto front of maximum lift coefficient and maximum lift-to-drag ratio, as illustrated in Fig. 38 (point P). This implies the existence of a group of dominating solutions with both better lift coefficient and lift-to-drag ratio. From the exploratory studies, it was concluded that an increase in these metrics is always beneficial in terms of trajectory performances, hence point P cannot be the optimum vehicle, which can only lay on the pareto front.

On the other hand, this does not imply that all the vehicles in the pareto front will have better trajectory performances than all the dominated solution. With reference to Fig. 39, assuming that the non-dominated solution (O) is the optimum vehicle in terms of trajectory performances, it is reasonable that a dominated solution with very similar performances (A) could display better trajectory performances than a non-dominated solution on one extreme of the pareto front (B), where the compromise between the two metrics is very far from

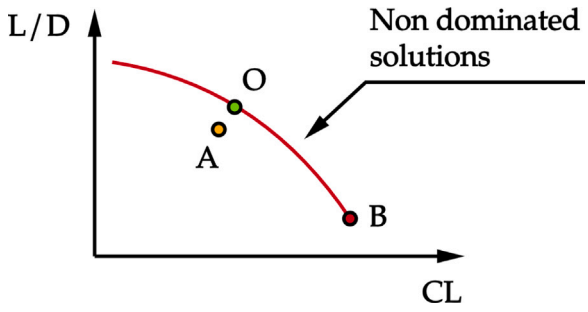

Fig. 39. Dominated solution A could display better re-entry performance than the non-dominated solution B.

optimal. What is implied is instead that for every vehicle which does not belong to the pareto front, it is possible to find a dominating solution with better trajectory performances.

This means that (with the already discussed hypothesis) it can be expected to find the optimum vehicle among the non-dominated solutions of a multi-objective wing shape optimization which:

1. Maximizes the maximum lift-to-drag ratio at Mach 14;
2. Maximizes the maximum lift coefficient at Mach 14;
3. Minimizes mass (in particular, the landing mass has been selected as mass metric).

The identification of the most performing vehicles is then performed in two-steps:

1. The identification of the non-dominated solutions of the three-objective wing-shape optimization.
2. Running simplified trajectory optimizations for all the vehicles of the obtained pareto front to assess the performances associated to each non-dominated combination of lift coefficient, lift-to-drag ratio and mass metrics. This will help identify the region of the pareto where the optimum is located, and ultimately locate the optimum itself (if unique).

5.1. Wing-shape optimization

The same optimization framework previously employed to optimize the SLP7 P2P trajectories (NSGA-III [20], implemented through the `pymoo` library in Python [47]) has been employed also for the wing-shape optimization, as it proved appropriate to tackle complex multi-objective optimizations with several control variables and constraints.

The following tables present the parameters that have been employed to setup the wing-shape optimization.

Variables	
First sweep angle `sw_1`	[55°, 80°]
Second sweep angle `sw_2`	[40°, 85°]
Tip chord `c_tip`	[2 m, 25 m]
Outside chord `l_out`	[0 m, 20 m]

Objectives	
Lift-to-drag ratio at Mach 14	Maximize
Lift coefficient at Mach 14	Maximize
Landing mass	Minimize

Constraints	
Maximum landing mass	150 t
Maximum landing speed	100 m/s
Geometry is consistent	True
Vehicle is flyable	True

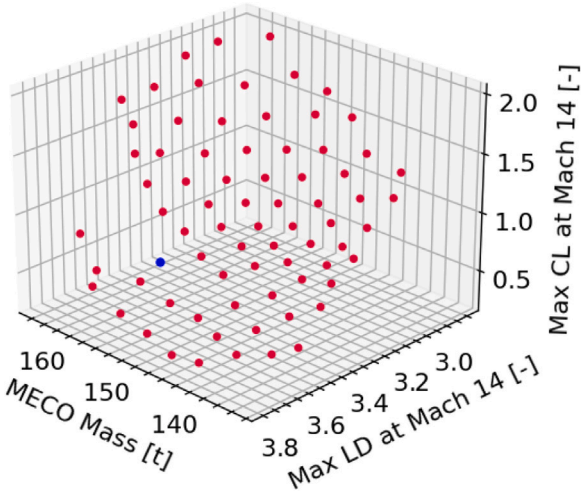

Fig. 40. Output pareto front of the three-objective wing-shape optimization and relative position of the SLP7 (blue dot).

NSGA-III Hyperparameters	
Target population size	500
Offspring population size	400
Crossover probability	0.5
Crossover eta	15
Mutation eta	40
Number of generations	450
Number of reference directions	120

Upon stabilization of the objectives, achieved around the 400th generation, convergence has been assessed by increasing the mutation rate and running the optimization for an additional 50 generations, to check whether the optimizer was stuck in a local minimum. The difference in the pareto fronts before and after the increase in mutation rate being small, the optimization has been considered converged. The obtained 3D pareto front is displayed in Fig. 40. The blue dot represents the SLP7 performances. As it already appeared from the parametric studies, the SLP7 confirms to be a non-dominated solution.

It may appear that a region of the pareto front is lacking solutions. NSGA-III retains the solutions of the objective space which are closest to a set of reference directions, distributed in such a way to ensure diversity in the selected solutions. In this case the reference directions are defined according to the Das and Dennis approach [48], which computes them by distributing reference points on a unit simplex in the normalized objective space, and then obtaining the reference directions by joining the origin (0, 0, 0) with each one of the reference points, as illustrated in Fig. 41.

Therefore, if the optimizer worked correctly, the solutions should be equally spaced when projected on the unit simplex along the line connecting the solution with the origin of the normalized objective space. This is indeed the case, as illustrated in Fig. 42, where we can observe the solutions uniformly spaced on the unit simplex, together with the vehicle geometry associated to each point of the pareto front (the red vehicle is the SLP7 geometry). Moreover, it was possible to determine which constraints and boundaries of the input variables shape the pareto front by studying their evolution along the pareto. This is also illustrated in Fig. 42.

5.2. Simplified trajectory optimizations

Each vehicle of the pareto front represents a different degree of (non-dominated) trade-off between the three optimized metrics. In order to find out which combination of lift-to-drag ratio, lift coefficient and mass metrics actually delivers the best trajectory performances,

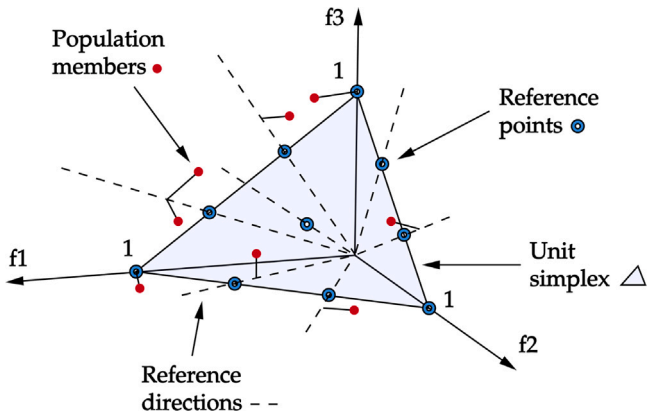

Fig. 41. Association of population members with reference directions in the case of three objectives ($f1$, $f2$ and $f3$). Reproduction from Figure 3 in Ref. [21].

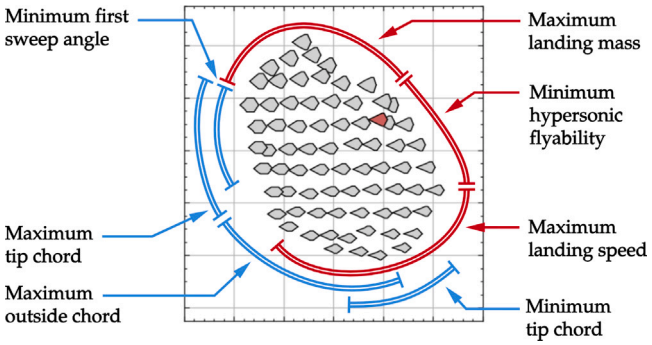

Fig. 42. Uniformly spaced solutions when projected on the pareto front, showing the vehicle geometry associated to each solution, and the constraints and input boundaries shaping the pareto front. Red vehicle is the SLP7.

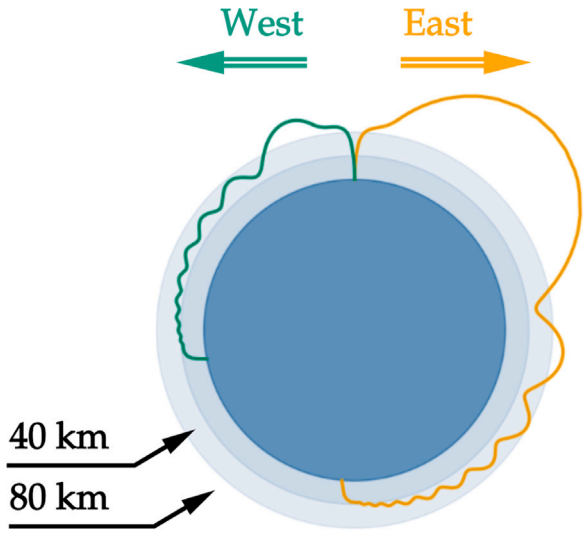

Fig. 43. Simplified trajectory optimizations launching from the equator towards a prescribed cardinal direction. Altitude magnification 25x.

each vehicle has been optimized along simplified trajectories, launching from the equator towards a prescribed cardinal direction, as illustrated in Fig. 43, maximizing the traveled distance for a constrained value of maximum re-entry heat flux.

In these simplified cases, the descent phase is controlled through two values of angle of attack: the maximum trimmable one at the beginning of the descent (skipping configuration), and the one granting the maximum lift-to-drag ratio at the end (gliding configuration). The optimizer can select at which instant of the atmospheric descent the vehicle shifts its attitude moving from one configuration to the other, as well as the duration of this shift in angle of attack. Moreover, the initial angle of attack at the beginning of the descent may also be used as a control variable of the optimization.

These optimizations, being single-objective and having a reduced set of controls and constraints, require considerably less time to be completed (less than an hour). They are therefore much more practical to be used to "quickly" assess trajectory performance, in place of the more computationally expensive P2P optimizations, while still allowing the evaluation of the effects of different launch azimuths, so to simulate P2P routes served in different directions. It is in fact remarked that a west-bound trajectory would impose a significant ΔV loss at the end of the ascent phase, thereby greatly reducing the achievable range. Moreover, a "blockade" constraint can be enforced to require the vehicle to fly at high altitudes (>80 km) in the initial part of the atmospheric descent, so to simulate the effect of including a minimization of the overflown population disturbance, while being less computationally expensive.

Variables	
Ascent phase pitching rate	[0.2°/s, 1°/s]
3 AOAs during ascent after stage separation	[−20°, 20°]
Descent time instant of AOA shift	[0 s, 4500 s]
Time duration of AOA shift	[0 s, 500 s]
(Optional) Initial angle of attack	[0°, 40°]

Objective	
Odometer (traveled ground distance)	Maximize

Constraints	
Maximum re-entry nz-load	1.5 g
Maximum dynamic pressure	40 kPa
Minimum altitude at 175 km downrange	80 km
Re-entry stagnation point peak heat flux	1.2–1.5 MW/m^2

NSGA-III Hyperparameters	
Target population size	500
Offspring population size	400
Crossover probability	0.3
Crossover eta	15
Mutation eta	20
Number of generations	100
Number of reference directions	13

Three types of simplified trajectory optimizations have been run, with different values of launch azimuths and maximum heat fluxes. Fig. 44 displays the obtained trajectories (one for each vehicle of the pareto front) for a westward launch with 1.2MW/m^2 of maximum re-entry peak heat flux.

Using again the pareto front projection on the unit simplex, and coloring each vehicle geometry according to its achievable range, a comprehensive visualization of the vehicles performance is obtained, as illustrated in Fig. 45.

These result allowed the identification of the three most performing configurations, which were then compared directly with the SLP7 on additional simplified trajectory optimizations, including the re-entry peak heat flux as a second minimization objective (for this reason the following results are 2D pareto fronts). Fig. 46 displays the comparison of the pareto fronts for the three most performing vehicles and for the SLP7 on a westward launch with no blockade constraint. As it can be observed, the SLP7 performance are dominated by the other three vehicles (this also holds for an eastward launch, with or without blockade),

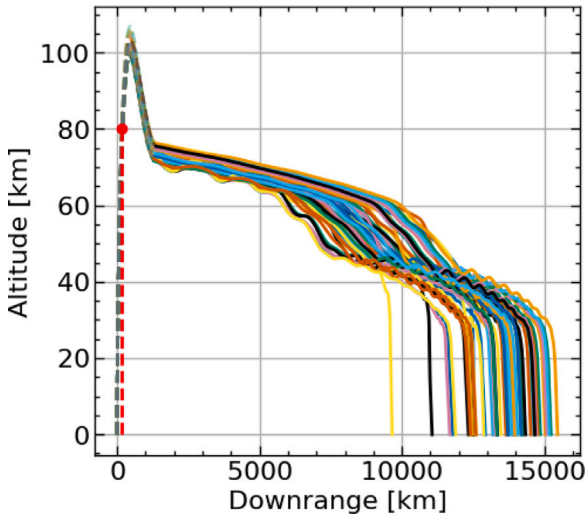

Fig. 44. Simplified trajectory optimizations systematically run on the set of non-dominated solutions of the wing-shape optimization.

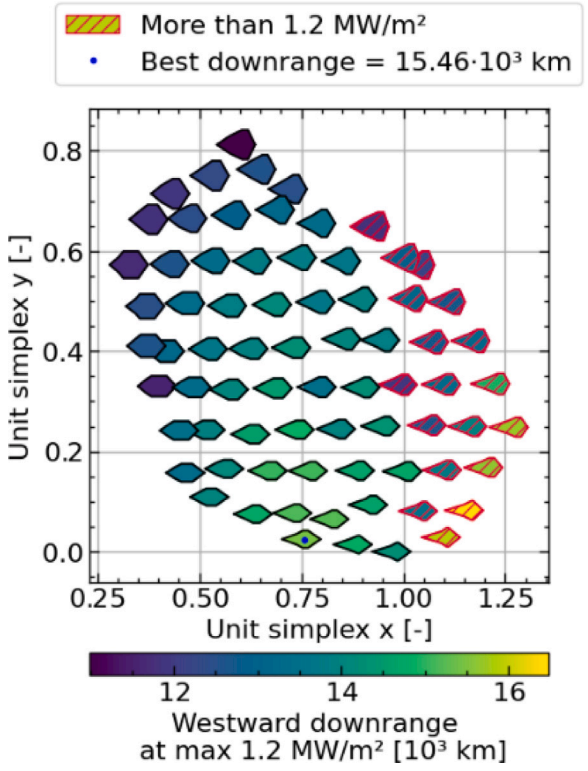

Fig. 45. Projected pareto front with vehicle geometry associated to each solution and achievable westward downrange with maximum 1.2 MW/m^2 of peak heat flux.

which is already a good sign that a more performing aerodynamic shape has been identified.

It is remarked how the obtained pareto fronts are monotonically increasing: a larger downrange is always obtained at the expenses of an increase in re-entry heat flux. This is the results of two trade-offs taking place simultaneously:

1. *Larger vs smaller entry angle of attack* - A large angle of attack at the atmospheric interface is associated to a lower lift-to-drag ratio and to an increased drag, which clearly results in a loss of downrange. On the other hand, the larger lift generated at high angle of attack allows the vehicle to fly and decelerate at higher altitudes in the initial portion of the flight (the one associated with the largest velocities), thus decreasing the heat flux. Conversely, smaller angles of attack in the neighborhood of the maximum lift-to-drag ratio will increase the achievable downrange, but higher heat fluxes will be withstood due to the trajectories diving faster into the denser parts of the atmosphere as a result of a lower lifting capability, as well as a reduced drag (i.e. slower deceleration).
2. *Gliding vs skipping trajectory* - For the same value of angle of attack, a gliding trajectory can achieve lower ranges with smaller values of heat flux, while the skipping ones can improve the achievable range at the expenses of higher peak heat fluxes (the vehicle digs deeper in the atmosphere at higher velocities).

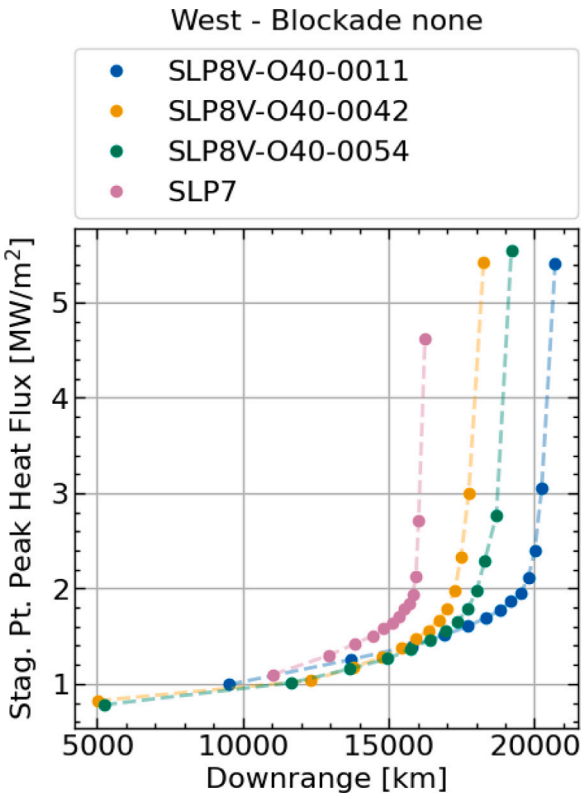

Fig. 46. Comparison of pareto fronts of most promising vehicles for a westward launch without the blockade constraint.

Amongst the three selected vehicles, the SLP8V−040−0011 is the one that can reach the farthest distances, but at the expenses of very large, non-admissible values peak heat flux. Moreover, due to its lower maximum lift-coefficient (even though it is fully trimmable at Mach 14), it cannot achieve as low heat fluxes as the other two vehicles for westward trajectories, with either no blockade or extended blockade. For these reasons this vehicle has not been retained for further analyses.

The remaining choice being between SLP8V−040−0054 and SLP8V−040−0042, it is observed how they have comparable trajectory performances as their pareto fronts are overlapping in the range of heat fluxes of interest (< 1.5 MW/m^2). Between these two vehicle with similar performance, the SLP8V−040−0042 has very similar values of the two sweep angles (≈ 70°), so that it can be considered for all practical purposes a single-delta wing. On the other hand, the shape of the wing leading edge of vehicle SLP8V−040−0054 (with a lower value of second sweep angle, i.e. two very well distinct wing segments) could lead to shock-boundary layer interactions that could locally increase the heat exchange [49], phenomena which are not modeled within HOTSOSE. Moreover, it can be assumed that the single-delta configuration

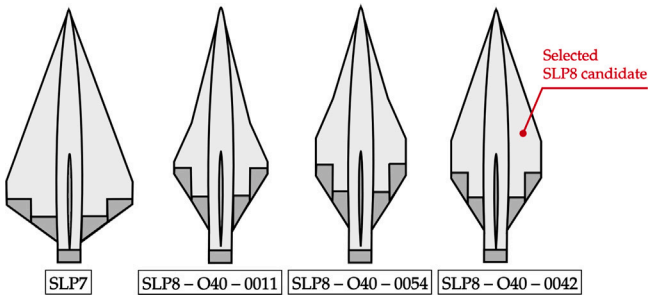

Fig. 47. Visual comparison of wing shape geometries between SLP7 and the three most promising aerodynamic shapes obtained from the wing-shape optimization.

Table 5
Comparison of wing-shape parameters between SLP7 and SLP8 candidate.

	SLP7	SLP8
First sweep angle	70°	71.6°
Second sweep angle	70°	70.1°
Tip chord	6 m	9.61 m
Outside chord	11.67 m	18.57 m

is advantageous also in terms of structural loads [50]. It could then be expected that the single-delta wing of vehicle SLP8V–O40–0042 could represent an advantage in terms of both heat transfer and structural loads, and for this reason this vehicle has been ultimately selected as a first candidate for the SLP8 configuration, and it will be the first one to be also trajectory-optimized along P2P routes. The geometries of the three most performing aerodynamic shapes obtained by means of the wing-shape optimization are pictured in Fig. 47, for a visual comparison with the SLP7 one.

Interestingly, all the three retained vehicles have a computed landing speed of just less than 100 m/s (the constrained maximum value within the wing-shape optimization, resulting from wear considerations on the landing gears [51]). This indicates:

1. That the maximum landing speed is the design-driving constraint, as it limits the pareto front in the region where the best trajectory performance are located. An increase in this value could allow vehicles with even smaller wings to fly and be able to land.
2. That the optimizer is working effectively, as it manages to explore the design space also in close proximity of the constrained values in order to find the most performing solutions.

For what concerns the comparison of geometries between the SLP7 and the SLP8 candidate, it is observed that:

- Both vehicles have a single delta wing with around 70° of sweep angle, which proves to be a good value granting large aerodynamic efficiency.
- The SLP8 candidate has smaller wings, implying a smaller vehicle mass.
- The SLP8 candidate has more forward-shifted wings, which provide better trim performances (improved relative position between the COG and the hypersonic COP). In fact, this vehicle can generate more lift at hypersonic velocities than the SLP7 despite its smaller wings as it is trimmable up to 64° of angle of attack at Mach 14 (while the SLP8 only up to 28°).

Table 5 displays the different geometrical parameters defining the wing shapes of the two vehicles, while Table 6 presents a comparison of the two vehicles in terms of the three relevant metrics (objectives of the wing-shape optimization).

It is concluded that the SLP8 candidate represents a much better compromise between these three metrics, as it trades-off a small loss in lift-to-drag ratio with a large increase in lift coefficient and a large decrease in vehicle mass.

Table 6
Comparison of three main performance metrics between SLP7 and SLP8 candidate.

	SLP7	SLP8	Difference
L/D at Mach 14 [–]	3.66	3.48	−5%
C_L at Mach 14 [–]	0.81	1.02	+26%
Landing mass [t]	151.5	133.4	−12%

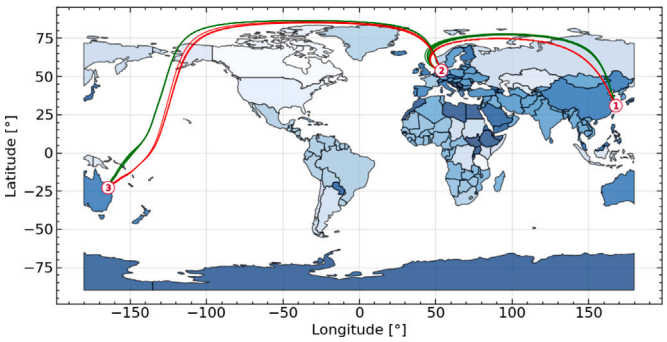

Fig. 48. Ground maps of the two optimized trajectories for SLP7 (green) and SLP8 candidate (red). The indicated location are (1) Shanghai, (2) Nordholz, (3) Australia.

Table 7
Comparison of P2P trajectory performance along the Nordholz to Australia route.

	SLP7	SLP8	Difference
Min. heat flux [MW/m^2]	1.53	1.04	−32%
Min. pop.disturbance [1e6]	0.36	0.22	−39%

Table 8
Comparison of P2P trajectory performance along the Shanghai to Nordholz route.

	SLP7	SLP8	Difference
Min. heat flux [MW/m^2]	1.06	0.85	−20%
Min. pop.disturbance [1e6]	0.92	1.17	+27%

5.3. Validation on P2P routes

Finally, the selected SLP8 candidate has been compared with the SLP7 along intercontinental routes of interest, including a computation of the overflown population disturbance using the same framework employed in [19]. Two routes have been analyzed:

1. The reference mission Europe to Australia.
2. A route from East Asia to Europe, for its economic importance, but also notably difficult to accomplish as it overflies largely populated areas.

Fig. 48 displays the obtained ground maps for the two vehicles along the two routes, while Tables 7 and 8 compare the point-to-point trajectory performances of the two vehicles.

As it can be observed, the SLP8 candidate always displays better trajectory performances, except for the minimum overflown population disturbance along the Shanghai to Nordholz route. A more detailed investigation of this case indicated:

- That the additional population disturbance associated to the SLP8 is connected to the overflying of a populated area in northern Russia (and not in East Asia).
- That the SLP7 always manages to avoid this area, but in order to avoid the populated regions close to Shanghai it requires a large initial skip associated to a much larger value of heat flux (1.64 MW/m^2 vs 1.26 MW/m^2 for the SLP8 candidate).

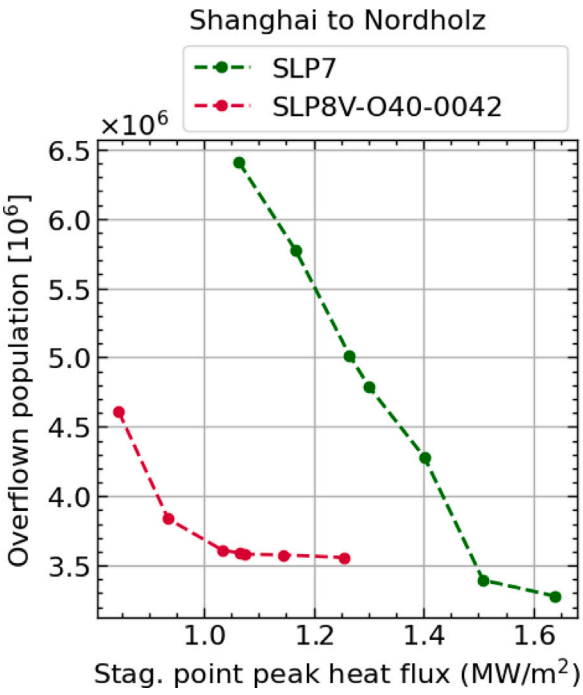

Fig. 49. Obtained pareto fronts along the Shanghai to Nordholz route.

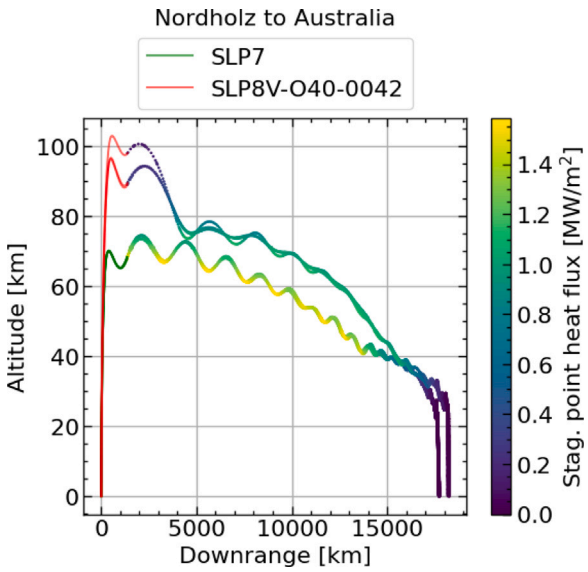

Fig. 50. Comparison of trajectories (altitude over downrange) along the route Nordholz to Australia. The color-map indicates the stagnation point heat flux during the atmospheric descent.

Comparing the output pareto fronts for this route, this situation corresponds to the left extreme of the green pareto, indicating trajectories where the SLP7 manages to disturb less population only by means of a large initial skip phase associated to very large values of re-entry heat fluxes, as illustrated in Fig. 49.

In any case, when restricting the analysis to acceptable values of heat flux (less or equal than 1.5 MW/m^2), the SLP8 performances strictly dominate the SLP7 ones along both the routes.

In order to better understand where this improvement in trajectory performance originates from, Fig. 50 displays the altitude over downrange plot of the optimized trajectories of the two vehicles along the Nordholz to Australia route, colored according to the re-entry stagnation point heat flux experienced during the atmospheric descent.

The convective heat exchange is modeled within **TOSCA** with a modified Chapman equation:

$$\dot{q} = 20254.4 \text{ W/cm}^2 \cdot \sqrt{\frac{\rho}{\rho_r}\frac{r_{n,r}}{r_n}} \left(\frac{V}{V_r}\right)^{3.05}$$

It is therefore proportional to the atmospheric density ρ and to the vehicle speed V (the value of nose radius r_n is identical for the two vehicles). The SLP8 candidate, by performing skips of lower amplitudes and at higher altitudes (both V and ρ are lower at the skip inflection point) can thus reduce the re-entry heat flux. Moreover, by flying at higher altitudes for a consistent portion of the flight, it can reduce the disturbance to the overflown populations. This high altitude trajectory with skips of low amplitudes is enabled by the increased lift coefficient and decreased mass of this vehicle, which largely compensate the small loss of lift-to-drag ratio with respect to the SLP7, ultimately allowing a substantial improvement of re-entry performance.

6. Conclusions

The objective of this work was the redesign of the SLP7-3 aerodynamic shape in order to allow it to fly both quasi-stationary gliding and skipping reentry missions. Thus, the vehicle will be capable of avoiding populated areas by either flying above them, at altitudes where the sonic boom will not reach the ground, or utilizing its hypersonic maneuverability to fly around them.

To tackle this complex multidisciplinary problem, an MDAO methodology was developed through the implementation of the following steps:

1. A decomposition of the design problem into two sub-problems (wing-shape optimization and trajectory optimizations), which were then coupled by an accurate selection of the objectives of the wing-shape optimization.
2. The development of SLOT to quickly assess a vehicle's trimmed aerodynamic and mass performance from a wing-shape parametrization.
3. An extensive exploration of the design space that allowed the simplification of the forthcoming wing-shape optimization.
4. The effective use of a multi-objective genetic algorithm to optimize the vehicle wing-shape.
5. The identification of the most promising SLP8 candidate amongst the obtained set of non-dominated solutions by means of simplified trajectory optimizations.

Finally, the expected improvement in re-entry trajectory performance was validated by comparing the selected new vehicle configuration with the previous design iteration along two P2P routes of interest, proving the effectiveness of the MDAO methodology.

It is also remarked how this MDAO was wider in scope and effectiveness than the ones previously implemented to optimize the SLP aerodynamic shape. In particular:

1. Trimmed aerodynamic performance were accounted for from the beginning and not assessed afterwards.
2. The aerodynamic shape was not optimized for the single lift-to-drag ratio objective, but for three contrasting objectives.
3. The design space was extensively explored, and the effects of constraints and bounds of the input variables understood. Moreover, the recurring trade-off between lift-to-drag ratio and lift-coefficient has been explained on the basis of the relative position between COG and COP, analyzing the movement of the latter as a function of the angle of attack.

4. The pareto front on non-dominated solutions of the wing-shape optimization was also analyzed and understood, and the most stringent, design-driving constraint was identified: the maximum landing speed.
5. The optimization did not consider only a single reference trajectory, but several ones. For the simplified case, both eastward and westward trajectories, with or without blockade constraints were analyzed. Then, two very different P2P routes were considered for the final analysis.

Moreover, despite the analysis being based on fast estimation methods, the obtained results were shown to be physically grounded. This was the result of an extensive post-processing of several intermediate results that were not blindly taken for granted.

Nonetheless, the results of such an analysis based on fast estimation methods have to be treated with care and have to be confirmed with more advanced and computationally expensive methods, ideally even with wind tunnel tests. The more detailed assessment of the identified promising configuration is currently ongoing. Special consideration will be given to the subsonic aerodynamic performance and trimmability, as the landing speed was identified as a critical constraint. Another area of interest is the re-assessment of the TPS for the new skipping mission type and wing shape.

In the future, SLOT functionalities shall be extended to include additional degrees of freedom in order to finalize the SpaceLiner 8 design, and ultimately SLOT's codebase is expected to be repurposed to perform the MDAO of additional vehicles.

CRediT authorship contribution statement

Tommaso Mauriello: Writing – original draft, Visualization, Validation, Software, Methodology, Investigation, Formal analysis. **Jascha Wilken:** Writing – review & editing, Supervision, Software, Methodology, Investigation, Conceptualization. **Steffen Callsen:** Supervision, Software, Methodology, Conceptualization. **Leonid Bussler:** Validation, Supervision, Methodology. **Martin Sippel:** Writing – review & editing, Supervision, Conceptualization.

Declaration of competing interest

The authors declare that they have no known competing financial interests or personal relationships that could have appeared to influence the work reported in this paper.

References

[1] M. Sippel, J. Klevanski, Preliminary Definition of Supersonic and Hypersonic Airliner Configurations, American Institute of Aeronautics and Astronautics, 2006.

[2] D. Neeb, T. Schwanekamp, Preliminary aerodynamic shape optimization of the SpaceLiner by means of engineering methods, in: 17th AIAA International Space Planes and Hypersonic Systems and Technologies Conference, San Francisco, California, 2011.

[3] T. Schwanekamp, B.C., A. Kopp, The development of the SpaceLiner concept and its latest progress, in: 4TH CSA-IAA Conference on Advanced Space Technology, Shanghai, 2011.

[4] M. Sippel, S. Stappert, Y.M. Bayrak, L. Bussler, S. Callsen, Systematic assessment of SpaceLiner passenger cabin emergency separation using multi-body simulations, in: HiSST: 2nd International Conference on High-Speed Vehicle Science Technology, Bruges, Belgium, 2022.

[5] ZEHST article 1, 2023, https://www.bbc.com/news/technology-33786999. (Last Accessed: 11 November 2023).

[6] ZEHST article 2, 2023, https://www.independent.co.uk/travel/news-and-advice/concordes-successor-revealed-at-paris-air-show-2300191.html. (Last Accessed: 11 November 2023).

[7] Destinus web page, 2023, https://www.destinus.ch/. (Last Accessed: 11 November 2023).

[8] Destinus S article, 2023, https://www.usinenouvelle.com/editorial/l-avion-hypersonique-a-hydrogene-de-destinus-soutenu-par-l-aeroport-de-rochefort-N2119536. (Last Accessed: 11 November 2023).

[9] Destinus L article, 2023, https://www.businessinsider.com/see-hypersonic-jet-will-fly-new-york-paris-90-minutes-2023-6?r=US&IR=T. (Last Accessed: 11 November 2023).

[10] Hermeus website, 2023, https://www.hermeus.com/. (Last Accessed: 11 November 2023).

[11] LAPCAT A2 article, 2023, https://www.theguardian.com/business/2008/feb/05/theairlineindustry.travelnews. (Last Accessed: 11 November 2023).

[12] Radian aerospace website, 2023, https://www.radianaerospace.com/. (Last Accessed: 11 November 2023).

[13] Space transportation article 1, 2023, https://trends.aeroexpo.online/project-78797.html. (Last Accessed: 11 November 2023).

[14] Space transportation article 2, 2023, https://dongfanghour.com/space-transporation-series-a/. (Last Accessed: 11 November 2023).

[15] SpaceX starship website, 2023, https://www.spacex.com/vehicles/starship/. (Last Accessed: 11 November 2023).

[16] Venus aerospace website, 2023, https://www.venusaero.com/. (Last Accessed: 11 November 2023).

[17] M. Sippel, O. Trivailo, L. Bussler, S. Lipp, C. Valluchi, Evolution of the SpaceLiner towards a reusable TSTO-launcher, in: 67th International Astronautical Congress, Guadalajara, Mexico, 2016.

[18] S. Candel, Concorde and the future of supersonic transport, J. Propuls. Power 20 (2004).

[19] S. Callsen, J. Wilken, S. Stappert, M. Sippel, Feasible options for point-to-point passenger transport with rocket propelled reusable launch vehicles, in: 73rd International Aeronautical Congress, IAC, Paris, 2022.

[20] D. Kalyanmoy, J. Himanshu, An evolutionary many-objective optimization algorithm using reference-point based non-dominated sorting approach, part I: Solving problems with box constraints, IEEE Trans. Evol. Comput. (2014).

[21] D. Kalyanmoy, J. Himanshu, An evolutionary many-objective optimization algorithm using reference-point based non-dominated sorting approach, part II: Handling constraints and extending to an adaptive approach, IEEE Trans. Evol. Comput. (2014).

[22] K. Dresia, S. Jentzsch, G. Waxenegger-Wilfing, et al., Multidisciplinary design optimization of reusable launch vehicles for different propellants and objectives, J. Spacecr. Rockets 58 (4) (2021).

[23] M. Balesdent, L. Brevault, B. Paluch, Multidisciplinary design and optimization of winged architectures for reusable launch vehicles, Acta Astronaut. 211 (2023) 97–115.

[24] A. Aprovitola, A. Viviani, L. Iuspa, G. Pezzela, Multidisciplinary design of reusable re-entry vehicles by optimization and computational fluid dynamics, in: 8th Eurpean Conference for Aeronautics and Space Sciences, EUCASS, Madrid, Spain, 2019.

[25] Z. Wang, W. Huang, L. Yan, Multidisciplinary design optimization approach and its application to aerospace engineering, Chin. Sci. Bull. 59 (2014) 5338–5353.

[26] L. Brevault, M. Balesdent, A. Hebbal, A. Patureau de Mirand, Surrogate model-based multi-objective MDO approach for partially reusable launch vehicle design, in: AIAA Scitech 2019 Forum, San Diego, United States, 2019.

[27] I.P. Sobieski, I.M. Kroo, Collaborative optimization using response surface estimation, AIAA J. 38 (2000).

[28] W. Hankey, Re-entry Aerodynamics, American Institute of Aeronautics and Astronautics, 1988.

[29] E. Sänger, J. Bredt, A Rocket Drive for Long Range Bombers, Technical Report, Technical Information Branch BuAer Navy Department, Ainring, 1944.

[30] J.D. Anderson Jr., Hypersonic and High-Temperature Gas Dynamics, second ed., American Institute of Aeronautics and Astronautics, 2006.

[31] F.J. Regan, S.M. Anandakrishnan, Dynamics of Atmospheric Re-Entry, Technical report, American Institute of Aeronautics and Astronautics, Inc., Washington, DC, 1993.

[32] N.X. Vinh, A. Busemann, R.D. Culp, Hypersonic and Planetary Entry Flight Mechanics, Technical report, University of Michigan, 1980.

[33] A.J. Eggers, H.J. Allen, A Comparative Analysis of the Performance of Long-Range Hypervelocity Vehicles, Technical report, National Advisory Committee for Aeronautics, 1958.

[34] S. Timoshenko, D.H. Young, Advanced Dynamics, McGraw-Hill, 1948.

[35] A. Miele, Flight Mechanics, Dover, 1990.

[36] J.H. Allen, A.J.J. Eggers, A Study of the Motion and Aerodynamic Heating of Ballistic Missiles Entering the Earth's Atmosphere At High Supersonic Speeds, Technical report, National Advisory Committee for Aeronautics, 1957.

[37] T. Mauriello, Multidisciplinary Design Analysis and Optimization of the SpaceLiner Passenger Stage (Master's thesis), Politecnico di Milano, 2023.

[38] J. Klevanski, M. Sippel, Beschreibung des programms zur aerodynamischen voranalyse CAC version 2, DLR IB 647-2003/04, 2003.

[39] U. Reisch, Th. Streit, Surface inclination and heat transfer methods for reacting hypersonic flow in thermochemical equilibrium, DLR IB 129-96/10, 1996.

[40] T. Durbin, G. Grossir, O. Chazot, Hypersonic aerodynamic predictions for arbitrary geometries using ANTARES, in: 2nd International Conference on High-Speed Vehicle Science & Technology, Bruges, Belgium, 2022.

[41] T. Schwanekamp, L. Morsa, G. Zuppardi, R. Molina, SART TN-026/2012 - SpaceLiner 7-2 Aerodynamic Reference Database, Technical report, Deutsches Zentrum für Luft- und Raumfahrt e.V. - Institut für Raumfahrtsysteme, 2012.

[42] H. Kayal, Aufbau eines vereinfachten simulationsmodells für den bahnaufstieg in der Groß kreisebene, DLR IB 318-93/05, 1993.
[43] D.M. Wolf, PEMDIT - ein computerprogramm zur massenabschätzung und geometrischen auslegung von transportsystemen, 1989.
[44] B.A. van der Rotten, A Limited Memory Broyden Method To Solve High-Dimensional Systems of Nonlinear Equations, (Ph.D. thesis), Mathematisch Instituut, Universiteit Leiden, The Netherlands, 2003.
[45] P. Virtanen, et al., SciPy1.0: Fundamental algorithms for scientific computing in Python, Nat. Methods 17 (3) (2020) 261–272.
[46] E.C. Polhamus, A Concept of the Vortex Lift of Sharp-Edge Delta Wings Based on a Leading-Edge-Suction Analogy, Technical report, NASA Langley Research Center, Hampton, VA, United States, 1966.
[47] J. Blank, K. Deb, pymoo: Multi-objective optimization in python, IEEE Access 8 (2020) 89497–89509.
[48] I. Das, J.E. Dennis, Normal-boundary intersection: a new method for generating the pareto surface in nonlinear multicriteria optimization problems, SIAM J. Optim. 8 (1998) 631–657.
[49] L. Bussler, S. Karl, M. Sippel, Shock-shock interference analysis for SpaceLiner booster, in: HiSST: 2nd International Conference on High-Speed Vehicle Science Technology, Bruges, Belgium, 2022.
[50] T. Schwanekamp, Implementierung eines Kopplungstools zur Optimierung der Aerodynamik und Aerothermodynamik, Technical report, DLR, 2010.
[51] J. Roskam, Airplane Design - Part IV: Layout Design of Landing Gear and Systems, The University of Kansas, Roskam Aviation and Engineering Cooperation, 1989.